First-Principles Modeling of Organohalide Thin Films and Interfaces

Edoardo Mosconi, Thibaud Etienne and Filippo De Angelis

Abstract Organohalide perovskites have emerged as a class of materials with a unique combination of optoelectronic properties, suitable for a plethora of applications ranging from solar cells to photoelectrochemical tandem cells, to lasing and lighting. Theoretical and computational modeling can deliver an hitherto inaccessible atomistic view of the crucial material properties and heterointerfaces ruling the operational mechanisms in all these devices. Here we present a unified view of recent activity in the computational modeling of interfaces relevant to perovskites solar cells. The performance of the proposed simulation toolbox along with the fundamental modeling strategies are illustrated using selected examples of relevant materials and representative interfaces. In particular, we discuss interfaces between the prototype methylammonium lead iodide perovskite with TiO_2 and ZnO semiconductors (acting as electron selective contacts in solar cells), exploring different surface terminations and doping by chloride ions. Also the effect of defects at the interface with TiO_2 is analyzed and their impact on solar cell performance is discussed. Finally, the heterogeneous interface between methylammonium lead iodide and water is analyzed, revealing dynamical hints on the perovskite degradation by water.

1 Introduction

Organohalide perovskites recently revolutionized the field of photovoltaics [1], and has been discovered that these materials are able to exhibit remarkable performances in terms of photocurrent generation. After lead–halide compounds were first suggested for photovoltaic applications in the 1980s [2, 3], one had to wait

E. Mosconi · T. Etienne · F. De Angelis (✉)
Computational Laboratory for Hybrid/Organic Photovoltaics (CLHYO), CNR-ISTM,
via Elce di Sotto, 06123 Perugia, Italy
e-mail: filippo@thch.unipg.it

E. Mosconi · F. De Angelis
CompuNet, Istituto Italiano di Tecnologia, Via Morego 30, 16163 Genoa, Italy

N.-G. Park et al. (eds.), *Organic-Inorganic Halide Perovskite Photovoltaics*,
DOI 10.1007/978-3-319-35114-8_2

2009 for Kojima et al. to report first actual use of perovskites for photovoltaics [4]. This first report has considerably gained interest and hence paved the way to a large number of contributions in the field, strongly motivated by the increasing performance of the light-conversion devices built from perovskites.

TiO_2 surface pretreatment prior to perovskites adsorption has further lead to a power conversion efficiency improvement from the firstly reported [4] 3.8 to 6.5 % [5], before the exploitation of spiro-MeOTAD hole transporting material (HTM) could lead to an increased performance (9.7 and 10.2 % PCE) and stability of the device [6, 7].

Design and material morphology monitoring advances then allowed for a significant improvement relatively to the PCE, with remarkable results coming up to 12, 15 and 15.4 % of PCE, respectively, performed by Seok and coworkers [8], Grätzel and coworkers [9], and Snaith and coworkers [10], which succeeded to obtain a planar heterojunction topography which, from a technological point of view, aroused considerable interest in particular in terms of reproducibility and stability of the built devices.

Up to now [11], the highest certified PCE and NREL efficiencies are now of 19.3 and 20.1 %, which places the perovskite solar cells technology as highly competitive in the field of photovoltaics when compared to known thin-film technologies [12].

Further technical improvement also allowed to investigate the more basic features of perovskite materials, such as optical and transport properties of methylammonium (MA) lead–halide perovskites [7]. Crystalline order markers could even be identified according to vibrational spectroscopy experiments [13, 14], and the importance of MA cation configuration space evolution in $MAPbI_3$ perovskites has also been highlighted by these means [15].

The diffusion length of photogenerated entities in $MAPbI_3$ at a micrometer scale has been revealed by photoluminescence and time-resolved UV-Vis absorption spectroscopy. These studies have actually evidenced low photogenerated species recombination rates in such materials, [16] which constitutes a highly desired feature for charge-separation-based photovoltaics. Similar systems, doped with chlorine [17] ($MAPbI_{3-x}Cl_x$) were also investigated with similar protocols. For these particular doped systems, it was showed that the charged entities generated by light-absorption are mostly free electrons and holes [18]. Hole (electron) transporting interfaces were also evidenced to show a singular ambipolar behavior of the photoactive perovskite material in solar devices [19, 20].

2 Tin and Lead Perovskites for Establishing a Reliable Computational Protocol

Structural properties of lead–halide perovskites are known to be reliably predicted by computational protocols involving the Generalized Gradient Approximation (GGA) of Density Functional Theory (DFT) [21–23, 36]. While the relevance of these DFT protocols is established for simulating geometrical structures, it is also

known that such level of theory is unable to provide transferable appropriate bandgap data, the latter quantity being most often underestimated by GGA-DFT. In particular, the previous statement holds for semiconductors and for ABO_3 perovskites. Some examples evidenced this underestimation, for instance ZnO, which bandgap is underestimated by about 2.5 eV when using GGA-DFT. A comparison has also been addressed between GLLB-SC and PBE functional for computing the bandgap of ABO_3 perovskites. In that case, PBE (a standard GGA exchange-correlation functional in DFT) has been shown to deviate from experimental data by ca. 0.5 eV.

Improvements in bandgap calculations by computational methods have been brought to the field, as for instance the use of hybrid xc-functionals (like B3LYP or HSE06 for example). Post-DFT methods were also used to increase the accuracy of theoretical bandgap predictions. Among these methods, we find the self-energy corrected GW approximation [24–28]. Note that hybrid functionals and GW methods have already been combined into a more elaborated computational protocol, which use for a perovskites bandgap benchmark lead to deviations remaining within a 0.2 eV [28].

On the other hand, lead perovskites bandgaps computed with GGA-DFT were shown to be in a good agreement with experiments, with for instance $CH_3NH_3PbI_3$ and $PbTiO_3$ bandgaps of [29, 30] ca. 1.30–1.60 and 1.68 eV computed theoretically, to be compared with the experimental values of [4, 7] 1.55 eV and [21] 1.70 eV, respectively. Unfortunately, the GGA-DFT protocol performance has been showed not to be transferable to tin-halide perovskites, for which the computed bandgaps were underestimating the experimental values [22, 31]. This is also true for $BaSnO_3$ and $SrSnO_3$ and, more generally, for structures of the type $ASnX_3$. However, in both cases, the relative bandgap difference is in agreement with experiments.

The low deviation between experimental and theoreticallead-based perovskites bandgaps has further [29, 32] been attributed to the lack of a proper treatment of electron correlation and relativistic phenomena (particularly important inPb atoms) in the calculations by GGA-DFT. These relativistic effects can be included in the calculation through the use of scalar-relativistic schemes or by evaluating the spin-orbit coupling (SOC). Therefore, it was suggested that the agreement observed between theory and experiments for this class of perovskites could be attributed to a fortuitous cancelation of errors taking place between electron correlation and SOC effects [32]. This was further confirmed by calculations involving large SOC magnitude [33].

At different temperatures, methylammonium lead and tin iodide perovskites have a tetragonal structure [34] with typical bandgaps at, respectively, 1.2 and 1.6 eV [34, 35], but while some tin iodide perovskites were shown experimentally to be able to perform hole transport [34, 36], methylammonium lead iodide and its chlorine-doped relative were shown to efficiently transport both holes and electrons [7, 37]. From these results, it appears that one of the key theoretical targets for the understanding of perovskites electronic structure is the elaboration of a reliable theoretical protocol able to retrieve optical and electronic properties of these

remarkable materials. Currently, SOC-GW calculations [38, 39] have been made affordable and are now able to correctly predict the optical, electronic and transport properties of methylammonium lead and tin iodide perovskites. These achievements actually pave the way to a reliable design of new perovskite structures for highly performant materials with outstanding conversion efficiencies [39].

3 Importance of the Interfacial Chlorine in TiO_2/Organohalide Perovskites Junction

Methylammonium lead iodide perovskites doped with chlorine, with a meso-superstructured and planar heterojunctions were shown to exhibit variable optical properties [18] and superior performances with respect to $MAPbI_3$ materials [10, 17, 40]. In a first stage, this performance improvement was attributed to carrier mobility, while it has been later attributed to lower reduced carrier recombination in chlorine-doped methylammonium lead iodide with respect to $MAPbI_3$ itself. Overall, the influence of chlorine in this performance enhancement remained uncertain. The structure of the material itself also remained unclear, though theoretical and experimental (X-ray diffraction) results pointed the possibility of a reduced chlorine inclusion into $MAPbI_3$ (one to four percents only) and low cell volume concentration (0.7 %) in $MAPbI_{3-x}Cl_x$ [41], which confirms the thermodynamically predicted low probability of solid $MAPbI_3$/$MAPbCl_3$ solutions formation [32, 42]. Mechanistic hypotheses were also introduced relatively to the perovskite growth assisted by chlorine in the doped MA lead iodide perovskite, while EDX (for Energy Dispersive X-ray analysis) measurments were unable to detect chlorine in the $MAPbI_3$ structure [43]. It was also reported that doping $MAPbBr_3$ with chlorine also enhances the photovoltaic performances without chlorine being detected by EDX, while still being present in the material according to XPS (X-ray photoelectron spectroscopy) analyses; it was therefore concluded that the chlorine species should be present at the vicinity or onto the perovskite/titanium oxide interface [44].

Though the chlorine-containing $MAPbI_{3-x}Cl_x$ perovskites were shown to have an oriented growth along the [110] direction (see Fig. 1), [8–10, 30, 40, 41, 43, 45–48] the $MAPbI_3$ perovskite on the other hand was globally exhibiting nonoriented structures, independently of the number of synthesis steps (one or two) [8, 9, 30, 43, 46–49]. Tentative explanations were involving the variable solvent (GBL or DMF/DMSO). The presence of a lead–chlorine precursor was also suspected as a possible reason for this growth variability. As multiple contributions [26, 50] have already highlighted the importance of perovskite morphology when relating it to charge-separation efficiency, cell stability [51, 52] and photovoltaic performances, one is now talking in terms of a so-called “chlorine effect”.

Theoretical electronic structure calculations were performed in order to assess the impact of the presence of chlorine on a prototypical TiO_2/perovskite junction. Those calculations have been performed on interfaces representative of mesoporous

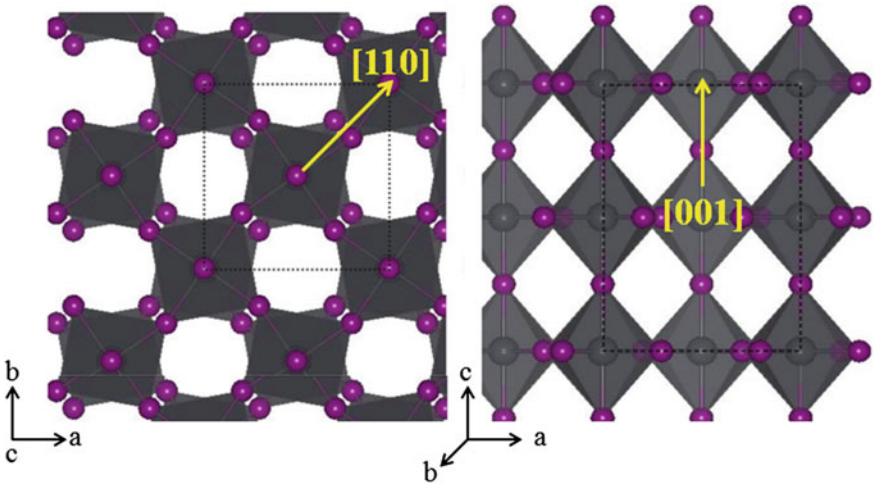

Fig. 1 Schematic representation of the methylammonium lead iodide perovskite X-ray structure projected along the *c* axis (*left*) and the *ab* plane (*right*)

and flat titanium oxide structure. The models were extracted from an optimized MA lead iodide structure, [32] obtained according to experimental X-ray data [29]. No symmetry constraint was used during these simulations, but the absence of inversion symmetry along the *c* axis was reproduced according to the I4 cm space group proposed previously for describing this system [30]. The lattice parameters of the tetragonal phase [53] were used for deriving the pseudo-cubic (001) and the tetragonal (110) surfaces. This means that since the tetragonal phase is representative of the actual structure of $MAPbI_3$ at room temperature, the simulations are aiming at reproducing reallistically this structure for the (110) surface. On the other hand (001) surface was also chosen for better reproducing the titanium oxide lattice. It should be noted that, however, these two surfaces share similar topology. Indeed, the (001) tetragonal phase surface matches with one out of the three (equivalent) cubic phase surfaces. As it has been established that SOC can be crucial to a proper theoretical treatment of Pb-perovskites electronic structure [33, 39, 54], and though scalar-relativistic (SR) schemes are correctly reproducing those properties [32, 39], spin-orbit coupling has been included into the simulation protocol protocol, while the GW approximation was not applied due to the system size, reducing the impact that GW could have on the calculations accurary.

According to a previous report related to the titanium oxide/perovskite heterointerface, the perovskite slabs have a 60:45:150 MA:Pb:I stoichiometry for a 3x5x3 scaffold as a starting model [55, 56]. This starting model has further been modified in order to include chlorine doping agent: fifteen I atoms were replaced by Cl ones at the interface, according to previous statements related to the hypothetical location of those chlorine atoms at the TiO_2/perovskite surface [41, 44]. The titanium oxide supercell for its part was simulated with the experimental cell parameters

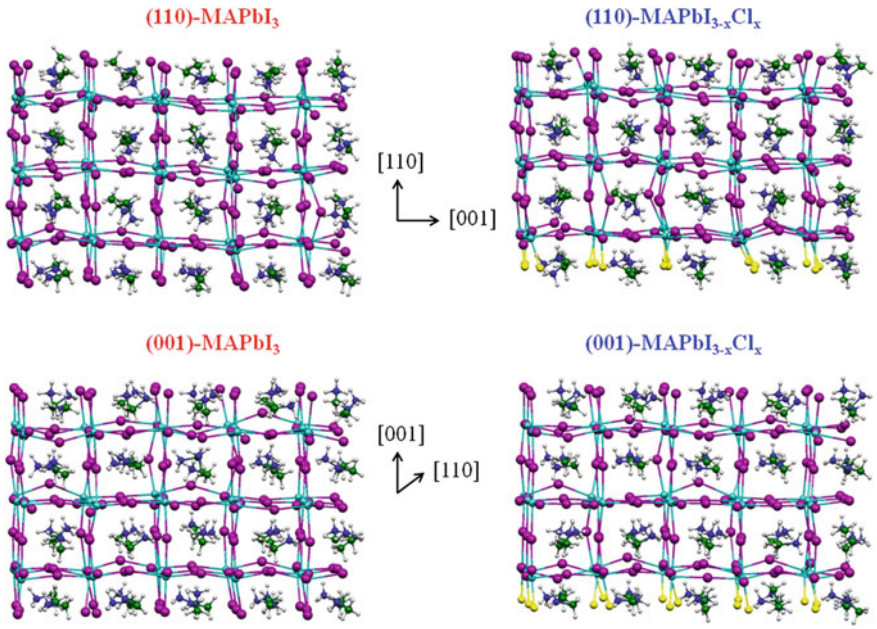

Fig. 2 Optimized structures of doped ($MAPbI_{3-x}Cl_x$—*right*) and undoped ($MAPbI_3$—*left*) (001) —*bottom*—and (110)—*top*—surface slabs

(a = 18.92 Å and b = 30.72 Å). An empty 10 Å space was also inserted along the nonperiodic direction, normal to the surface. The structure of the (110) and (001) slabs surfaces of doped and undoped perovskites are displayed in Fig. 2.

The outcome of these investigations can be summarized as follows: The bandgap for the optimized (110) methylammonium lead iodide slab calculated with (SOC-DFT) and without (SR-DFT) including spin-orbit coupling are, respectively, of 1.32 and 1.96 eV, and from a structural point of view only +0.36 (*a*) and +1.92 % (*b*) deviations along the titanium oxide directions for the (110) surfaces were obtained, while for the pseudo-cubic surfaces (001) those values are of +0.75 and −1.85 %. It was also deduced that a −6.40 and −13.52 % structural deviation is obtained from calculations for the tetragonal (001) surface with the same titanium oxide slab. The use of experimental $MAPbI_3$ (110) surface's cell parameters on another hand induced a 0.4 eV total energy decrease (corresponding to a 1.87 eV bandgap). This has lead to the conclusion that a minimal structural strain in the simulation is responsible for the variations between the two simulated structures. Moving from extended to finite system has also expectedly [31] introduced an upper bandgap shift for the bulk tetragonal $MAPbI_3$ phase. It was further showed that when the size extension of the perovskite slab is doubled along the nonperiodic [110] direction, a 1.55 eV bandgap value is found with SR-DFT for the (110) surface, which can be compared to the one obtained for the bulk with identical protocol. Scalar-relativistic and SOC-DFT delivered larger bandgap values

(2.37 and 1.50 eV, respectively) for the methylammonium lead iodide (001) surface. As a consequence to the fact that chlorine doping agents only introduce occupied levels below the VB (Valence Band) edge, [32] substituting iodine with chlorine did not actually have an impact on the bandgap.

Both undoped and chlorine-doped $MAPbI_3$ have a higher stability with (110) surfaces. Actually, titanium oxide increases the stability of such surface according to a favorable relative configuration between undercoordinated Ti atoms and the halide atoms on perovskite surfaces. The observed time stability enhancement of doped cells was then partly assigned to the increased binding energy between perovskite and titanium oxide, due to the presence of these interfacial atoms. Moreover, it was showed that titanium oxide-doped perovskite interfacial interactions have an impact on the electronic structure of titanium oxide. In particular, increased coupling between Pb *p* and Ti *d* conduction band states were evidenced theoretically. The titanium oxide conduction band was also showed to be slightly upshifted. More importantly, it has been reported that interfacial chlorine produces a conduction band edge asymmetry in chlorine-doped $MAPbI_3$ with respect to its undoped relative. This actually leads to an enhanced charge-transfer between the $MAPbI_{3-x}Cl_x$ structure and titanium oxide, which can explain the importance of the light-absorption generated electrons flow in direction of the titanium oxide surface.

4 PbI_2-Modified TiO_2/$MAPbI_3$ Heterointerface Electronic Coupling

As underlined in various contributions, a proper understanding of structural and electronic features of the perovskite/titanium oxide junction properties is of seminal importance for optimizing functional devices [55, 57, 58]. Unfortunately the characterization of this mesoporous interface by experimental techniques still remains quite challenging, even if levels alignement were already studied by means of XPS/UPS and EBIC [20, 59–61]. Unfortunately, though the current energetic features of these materials at the interface are quite favorable for photocurrent generation, the charge-separation at the heterojunction is still not optimal [62, 63] which results in some undesired charge accumulation phenomenon.

Some investigations are reporting how titanium oxide-containing $MAPbI_3$ perovskite cell stability, efficiency and hysteresis could be improved by using non-stoichiometric ratio for the MAI:PbI_2 precursor. Ten to twenty percentage of PbI_2 excess were reported [6, 64] to bring a desired effect for photovoltaic applications with respect to the one-to-one ratio. A recent combined experimental/theoretical study [65] has reported on the effect of PbI_2 on the heterojunction electronic properties, assuming that the PbI_2 excess remains in the vicinity of the interface, and showing that the presence of this excess favorably modifies the energy levels alignment and the interfacial electronic coupling, which can ease the interfacial electron transfer and might help to prevent a fast quenching, unlike for the 1:1 precursor. Micro-Raman measurements have suggested that the PbI_2 in

excess can also impact the crystallization dynamics. These data together with SEM imagery have confirmed that the excess of PbI_2 is homogeneously distributed possibly at the titanium oxide/perovskite interface.

Tetragonal (110) $MAPbI_3$ surface was then simulated by means of SOC-DFT electronic structure method, based on a scalar-relativistically optimized structure, under two forms: MAI- and PbI_2-terminated $MAPbI_3$, the latter representing the PbI_2-rich growth conditions. These structures were further placed in contact with a 120 titanium oxide anatase 5 × 3 × 2 slab, with a mostly exposed (101) surface (see Fig. 3). The supercells structures were built by using TiO_2 cell parameters, for a lattice deviation not exceeding two percents. Again, it was showed that the methylammonium–iodine termination of perovskites is responsible for interfacial interactions, implying iodine into a binding mode with undercoordinated surficial titanium atoms. For the lead–iodine-terminated perovskite on the other hand, the junction interactions were shown to occur through the formation of lead–oxygen and iodine–titanium interactions, as reported in Fig. 3.

Each scaffold was shown to be possibly existing, as only a slight (less than 0.1 eV) binding energy difference was deduced from the calculations. As far as the electronic properties of the two interfaces are concerned, though one is aware that the theoretical protocol cannot retrieve the adequate level alignment, still a proper relative effect arising from the various surface terminations is expected to be reliably treated during the simulations. The MAI-terminated $MAPbI_3$ conduction band

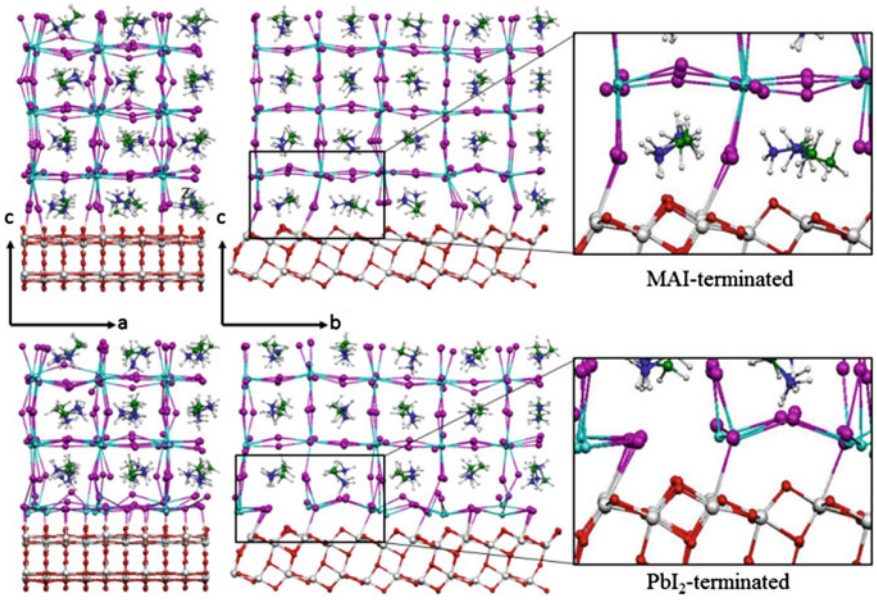

Fig. 3 (110) Titanium oxide/perovskite interface (optimized structures) for methylammonium-iodine-terminated (*top*) and PbI_2-terminated (*bottom*) agencements. *Light* and *dark blue colors* are pointing the lead and nitrogen, while *purple*, *green* and *white* are, respectively, pointing iodine, carbon and hydrogen

edge was calculated to be at around 0.8 eV, with a deviation of 0.4 eV with respect to the experimental value [59]. One could notice from the theoretical results that while the VB and CB are slightly down-shifted when going from the methylammonium-iodine to the lead–iodine-terminated interface. Unlike the former, for which a sharp CB edge has been obtained, the latter actually exhibits a tail of perovskite states remaining at approximately one electronvolt below the main CB window. From these results one can conclude that there exists an improved electronic coupling between perovskite and titanium oxide in the case of lead–iodine-terminated structure. This has been attributed to the reduced distance (2.8 Å, to be compared with 3.3 Å) between lead *6p* and titanium *3d* states in the case of lead–iodine-terminated structure. These two states were considered for comparison, as they are the main constituents of the perovskite and titanium oxide conduction bands. Since the electronic coupling is known to decay exponentially with the distance, such a slight distance variation can induce a substantial coupling shift. Density of states (DOS) calculations (see Fig. 4) have been reported to highlight the fact that unlike for methylammonium–iodine termination, the conduction band bending obtained for the lead–iodine one is more substantial. This is representative

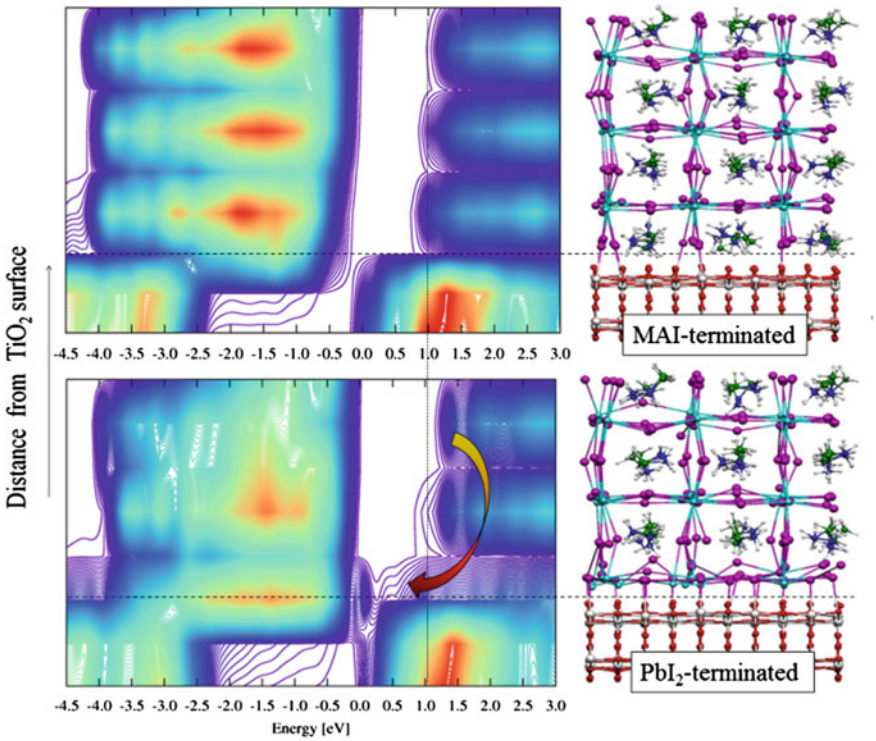

Fig. 4 Isodensity plot of integrated density of states, reported with respect to the distance from anatase surface. Increased DOS values are represented by a *blue-to-red* color variation. In the case of lead–iodine termination panel (*bottom left*) the arrow points the band bending

of a stronger coupling, which is in good agreement with the previous conclusions (see above), and with a predicted enhanced interfacial charge injection, as experimentally reported.

5 $MAPbI_3$ Thin Films Deposited on Zinc Oxide—a Thermal Instability Survey

Though perovskite solar cells are known to constitute a highly promising alternative for renewable energy technologies, the devices built from such materials are still suffering from film instability and hence reduced device lifetimes. As for third-generation solar cells, various possibilities exist for depositing perovskite material onto a surface when mounting a photovoltaic device. Among these options one finds for instance titanium oxide (TiO_2), indium tin oxide (ITO) or zinc oxide (ZnO).

A recent joint experimental/theoretical investigation [66] reported on the thermally annealed zinc oxide/$MAPbI_3$ films by means of in situ absorbance spectroscopy and grazing incidence X-ray diffraction (GIXRD) and density functional theory calculations. This survey allowed to elucidate the decomposition mechanism of the deposited perovskite, which has been shown to be caused by acid/base reaction at the heterojunction: with time, the MA cation deprotonation occurs and leads to the formation of CH_3NH_2. This was partially assigned to the basicity of zinc oxide surface, which has been shown to be reduceable by a preliminary annealing treatment of the zinc oxide film, taking place before depositing $MAPbI_3$. Such a problem is less likely to be encountered in titanium oxide or ITO-containing devices, as these surfaces appear to be more acidic than zinc oxide.

These experimental deductions were further confirmed by a computational analysis performed on the zinc oxide/$MAPbI_3$ interface [55, 57], with a comparison given with respect to interfaces substituting zinc oxide by titanium oxide. To this end, a $3 \times 5 \times 3$ tetragonal slab of $CH_3NH_3PbI_3$ was deposited onto a $6 \times 6 \times 3$ wurtzite ZnO slab. The former slab exposes its (110) surface while the zinc oxide slab exposes its apolar (1010) surfaces. The structural deviations (lattice mismatch) were showed to be very low (1.7 % for *a* and 2.3 % for *b* cell dimension). In both cases the perovskite material displays an orientation exposing the MAI terminations to the surfaces, which highly favors iodine–metal (undercoordinated zinc or titanium) bond formation, as well as MA-O hydrogen bonds formation. Scalar-relativistic geometry optimization of the zinc oxide/$MAPbI_3$ junction leads to a 19.5 eV interaction energy with evaluating the joint and isolated systems energy difference. This value can be compared to the 24.2 eV one for titanium oxide/$MAPbI_3$ [57]. These data actually correspond to a 1.3 eV (ZnO) and 1.6 eV (TiO_2) energy value per undercoordinated metal atom. One can therefore deduce from these theoretical results that the perovskite deposition on ZnO is less effective than the one on titanium oxide.

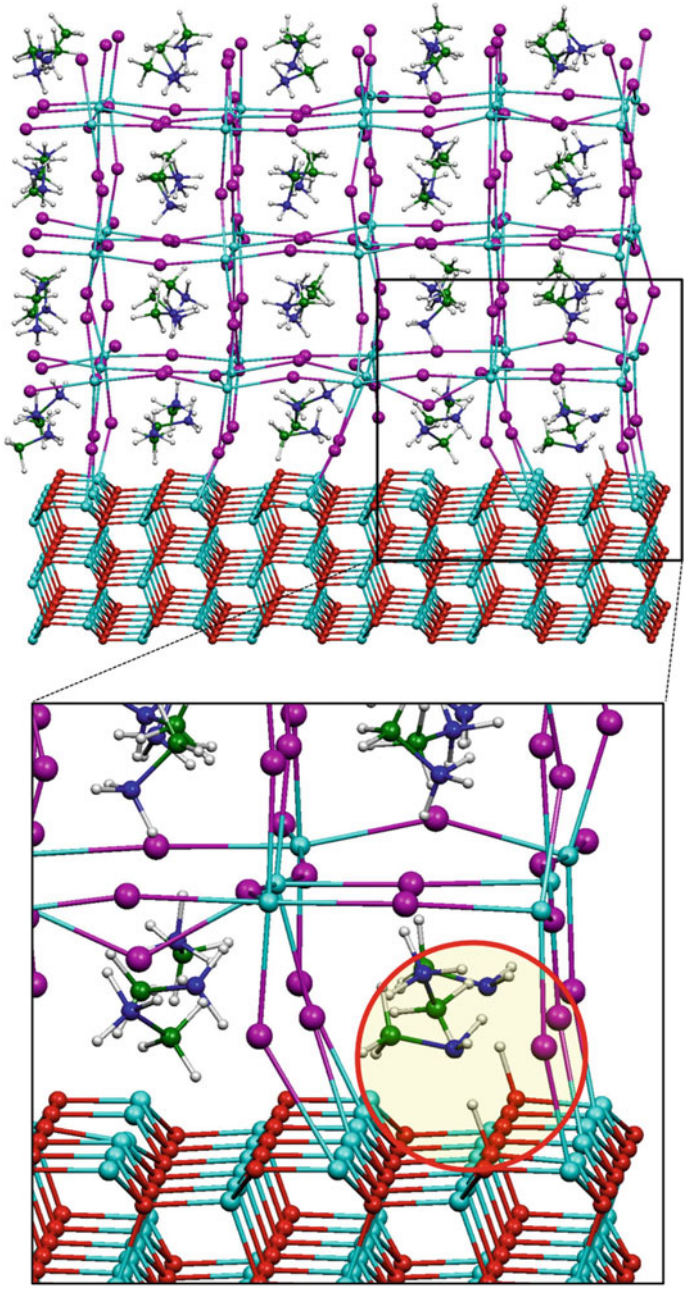

Fig. 5 Zinc oxide/$MAPbI_3$ heterojunction structure, optimized by scalar-relativistic DFT. *Bottom pannel* is a zoom of this structure, intending to evidence the MA deprotonation by an oxygen atom from zinc oxide

Moreover, it was noticed that for the zinc oxide/perovskite interface, two (out of fifteen) MA species have been deprotonated during the relaxation, leading to methylamine. The two protons extracted during the deprotonation process are present, adsorbed on zinc oxide by oxygen atoms. Four MA entities out of 15 have been shown to be deprotonated when the $MAPbI_3$ (001) surface is exposed to the zinc oxide slab. On the other hand, deposition of $CH_3NH_3PbI_3$ onto a titanium oxide slab did not exhibit such feature [15], confirming the difference in acidity properties between the two slabs. Figure 5 displays an optimized $CH_3NH_3PbI_3$ structure, with a zoom graphically evidencing the deprotonation of a methylammonium cation by vicinal zinc oxide oxygen atom.

Note that besides these results consolidating the mechanistic hypothesis responsible for the deposited film thermal instability, further experimental characterizations have been carried out in the same contribution in order to assess the influence of interfacial hydroxyl groups or the presence of residual organic ligands.

6 Defect Migration in $MAPbI_3$ and Its Effect on the $MAPbI_3/TiO_2$ Interface

Among the various limitations encountered when developing new perovskite cell devices, one often cites the J-V curves hysteresis phenomenon or the slow photoconductivity response. A possible feature at the origin of these undesired phenomena could be the ion/defect migration, which is an often referred hypothesis. In order to unravel the impact of defect migration on the properties of the perovskite solar cells, a theoretical study was conducted [67] on the titanium oxide/methylammonium lead iodide perovskite interface. Tetragonal supercells were used to evaluate some previously reported most probable $MAPbI_3$ defects [68–72] migration energetics. A very low (ca. 0.1 eV) activation energy was found for iodide vacancies and interstitial defects, while a 0.5 eV and 1.0 eV value has been attributed to the migration of the methylammonium and lead, respectively. It has been concluded from the simulations that the fast iodide defect migration are unlikely to be responsible for the slow $MAPbI_3$ response, while on the other hand the migration of methylammonium vacancies could be an explanation. A quantitative model was elaborated in order to explain the defects migration by locating the preferential defects at the vicinity of the interface with titanium oxide.

A simulation cell [13] was created with thirty-two $CH_3NH_3PbI_3$ units (for a total of 384 atoms). For the sake of comparison, similar calculations have been performed on $MAPbBr_3$ by using pseudo-cubic cell parameters. A migration path was modeled in order to determine the hypothetical defect migration through the perovskite crystal for the four types of defects studied (see Fig. 6). Saddle points were also located. In the following, vacancies will be pointed by a "V" while interstitials will be assigned by an "i" subscript, substitutions by MA_{Pb} or Pb_{MA} and anti-site substitution by MA_I, Pb_I, I_{MA} and I_{Pb}.

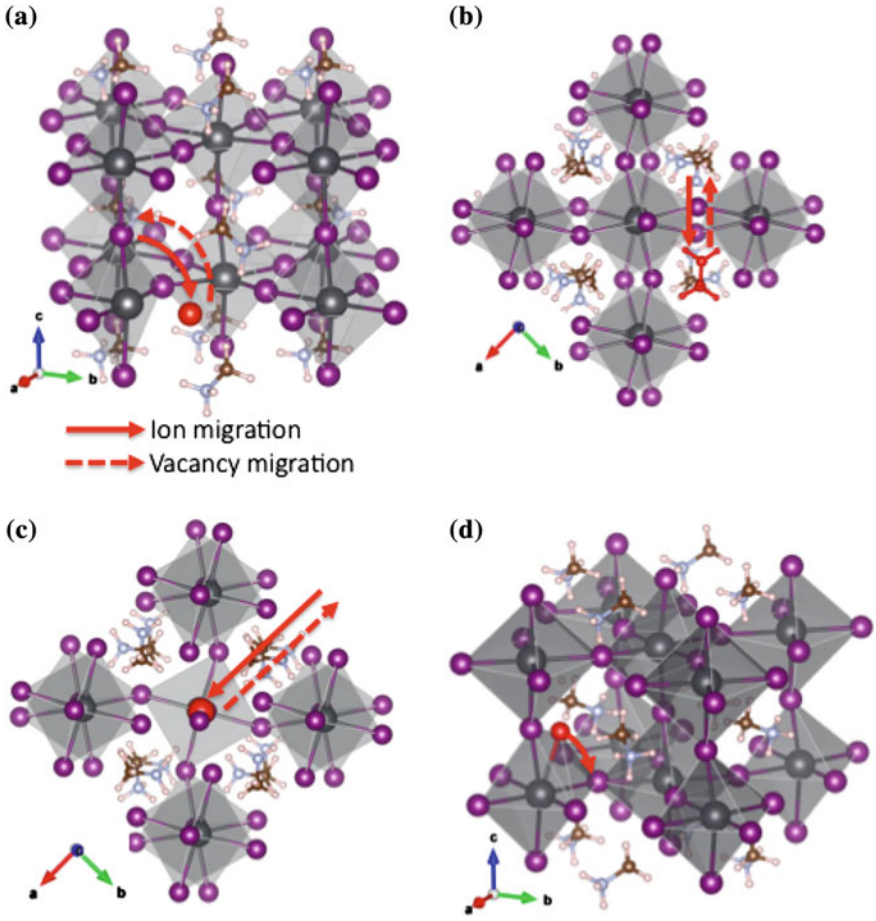

Fig. 6 **a** V_I, **b** V_{MA}, **c** V_{Pb} and **d** I_i defects diffusion paths. Ions (vacancy) migration pathways are represented by *solid* (*dashed*) *lines*. The *white color* is used for pointing hydrogens, *brown color* for carbons, *blue* for nitrogen, *purple* for iodine, *black* for lead atoms

The iodide vacancies (V_I) were simulated by generating a vacancy in an equatorial position. This vacancy was then allowed to migrate in the direction of an axial site (Fig. 6a) Unlike V_I which exhibits iso-energetic axial/equatorial sites migration, the axial and equatorial sites are not iso-energetic for the vacancies of bromine (V_{Br}), with a difference of 0.07 eV in favor of the axial site. As far as the methylammonium vacancies (V_{MA}) are concerned, the inter-site vacancy hopping is occuring between two adjacent cavities, located in the *ab* plane (Fig. 6b). Similarly, lead vacancies (V_{Pb}) are migrating along the four-lead-iodide atoms square (Fig. 6c). As far as iodide interstitials (I_i) are concerned, it has been shown that, similarly to V_I, those are following a path along the *c* axis (see Fig. 6d). It is important to note that for these analyses, a similar migration energy has been

Table 1 Activation energies (E_a, expressed in eV) and rate constants (k, in s^{-1}) related to defects migration in $CH_3NH_3PbX_3$ (X = I, Br)

	$MAPbI_3$		$MAPbBr_3$	
Defect	E_a (eV)	k (s^{-1})	E_a (eV)	k (s^{-1})
$V_{I/Br}$	0.08 (0.16)	1.7×10^{12} (7.7×10^{10})	0.09	1.2×10^{12}
V_{MA}	0.46	6.5×10^{5}	0.56	1.3×10^{4}
V_{Pb}	1.06	4.6×10^{-5}	–	–
I_i	0.08 (0.16)	1.7×10^{12} (7.7×10^{10})	–	–

The values reported in parentheses for the methylammonium lead iodide material are referring to the activation energies and rate constants of two consecutive hopping events

attributed to various defects corresponding to identical chemical entities. For instance, pathways implying the methylammonium migration (MA_{Pb} or MA_i) are characterized by an activation energy similar to the one obtained for V_{MA}. As a matter of fact, the V_I and I_i activation energies were deduced to be equal. Obviously, a similar reasoning also takes place for methylammonium lead bromide perovskite material.

We see in Fig. 6 that path length of V_{MA} and V_{Pb} is twice the one of V_I and I_i. In other terms, the two first will travel along one unit cell while V_I and I_i hop along half a cell. As a consequence, and in order to have a proper comparison of the four processes, the iodide-related activation energies were doubled, which actually corresponds to two hopping actions taking place consecutively. The activation energies (E_a) were calculated for the various defects migration and are displayed in Table 1, and can be placed into the Arrhenius equation in order to evaluate the migration rate:

$$k = \frac{k_B T}{\hbar} e^{-\frac{E_a}{RT}} \tag{1}$$

The main conclusions that can be drawn from reading Table 1 can be expressed as follows: the migration of lead vacancies (V_{Pb}) in $MAPbI_3$ can be regarded as a slow process, while the methylammonium vacancies diffusion is reported to have a 0.46 eV energy barrier, which is in good agreement with the 0.45 eV value deduced experimentally [73]. On the other hand iodide vacancies and interstitials are predicted to have a very flat energy pathway.

If one is now interested in comparing the methylammonium lead bromide and iodide structures, it can be seen that higher hopping activation energy is found for iodide vacancies than for bromide vacancies. We also see that MA migration between two unit cells is more difficult for iodide-containing material.

Without any field, the defects bearing a charge would travel along a random migration path through the perovskite layer. If one observes the symmetric energy landscape (see Fig. 7a), we see that backward and forward defect motions cannot be differentiated in any given crystallographic direction. In working conditions there exists a photogenerated field, which favors the migration of charged defects in the direction of the side of the perovskite film in contact with the so-called hole/electron

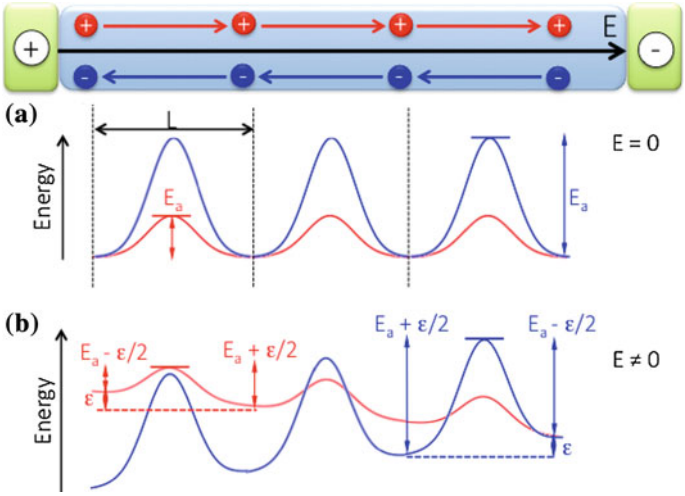

Fig. 7 Energy landscape of iodide (*red*) and methylammonium vacancies (*blue*) migration, at zero (**a**) and non-zero (**b**) electric field

transporting layer (HTL/ETL). The defects get stabilized through their path toward the selective contacts, which is explained by a higher interaction of electrostatic nature with the electrode. This stabilization, written ε/2 independent on the activation energy for defects sharing the same charge, and estimated to ca. 2 meV in cell working conditions, can be seen as a migration driving force. From this assumption, one could state that for $MAPbI_3$ this driving force is reducing (increasing) the activation energy of direct (reverse) migration by a ε/2 factor at the transition state (see Fig. 7b). One can deduce from these results that the predicted forward hopping event kinetics are twice faster than those of the backward one.

Note that the time for iodide vacancies or interstitials defects in the middle of a perovskite layer of 300 nm to reach the selective contact has been estimated to be of the order of tens of nanoseconds, which is actually faster than usual photovoltaic measurements scanning rates. On the other hand, methylammonium vacancies would reach the ETL in tens of milliseconds, which can be seen as possibly affecting the J-V measurements, and can constitute an hypothetic cause for the slow response and hysteresis in perovskite solar cells. Finally, lead vacancies were shown not to be mobile enough for affecting the cell operation.

As it is now established that in bulk $CH_3NH_3PbI_3$ the most mobile defects are iodide vacancies and interstitials, as well as methylammonium vacancies, this assumption allows to draw further conclusions related to the influence of their motion on the overall cell functioning (see Fig. 8) with a focus on the migration of iodide and methylammonium in particular, due to its reported low energy cost of 0.08 eV [71].

In working conditions, the cell will exhibit an electric field induced by light-absorption, pointing from ETL to HTL (e.g., from titanium oxide to Spiro-MeO-TAD-coated Au—see Fig. 8a). This field will induce the motion of

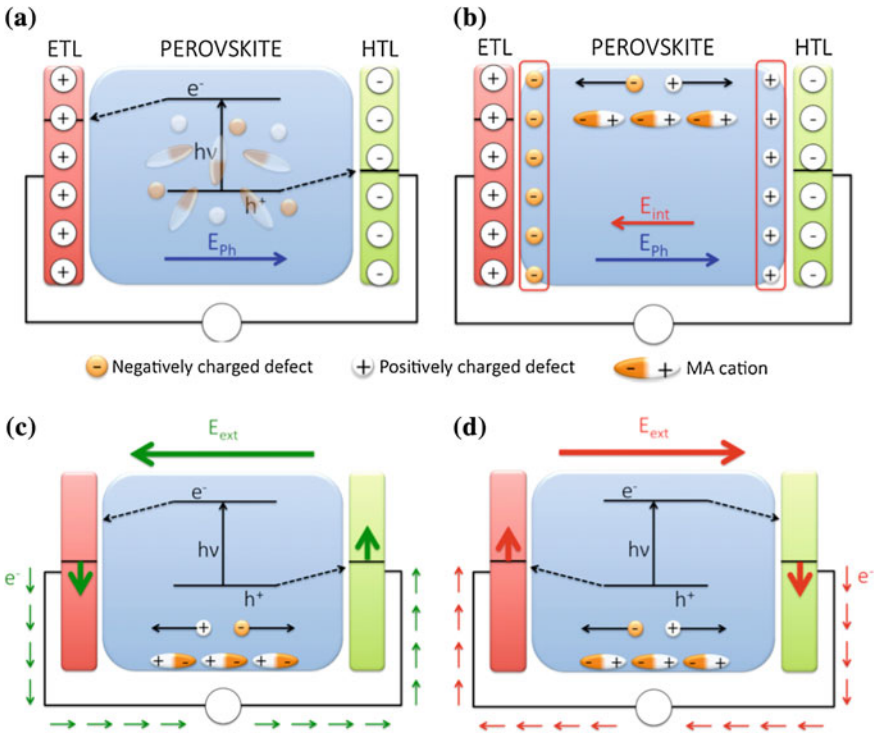

Fig. 8 Defect migration sketch: **a** photogenerated potential-induced charge carriers separation and even point defects distribution, random MA cations orientation; **b** MA cations point defects migration and reorientation, in response to absorption generated field (E_{Ph}) and the induced internal potential (E_{int}); (**c**, **d**) poling: switchable current as a function of the applied field

iodide (MA) vacancies toward HTL (ETL), as shown in Fig. 8b. Therefore, an accumulation of these migrated defects will induce the generation of an electrostatic potential across the $MAPbX_3$ film, in the opposite direction to the one generated by photon absorption and driving the charge-separation in the cell, which impacts the transport properties, hence the performance of the functioning cell.

Additionally, it might be noticed from Fig. 8b that the methylammonium cations can undergo a reorientation in response to the photoinduced field, causing an additional contribution to the defects-generated internal potential.

Note that it was hypothesized [74] that positive (negative) charge defects develop states close to (above) the perovskite CB (VB), inducing an n(p)-doping of the perovskite in contact with the anode (cathode). Positive poling (Fig. 8c) makes the cell to behave like an n-i-p junction. The current will therefore follow the perovskite doping-created gradient. On the other hand, negative poling makes the cell to behave like a p-i-n configuration (Fig. 8d).

The electronic structure of (110) perovskite slab in contact with a (101) titanium oxide slab (anatase) was calculated (see Fig. 9a). The V_I (V_{MA}) diffusion toward

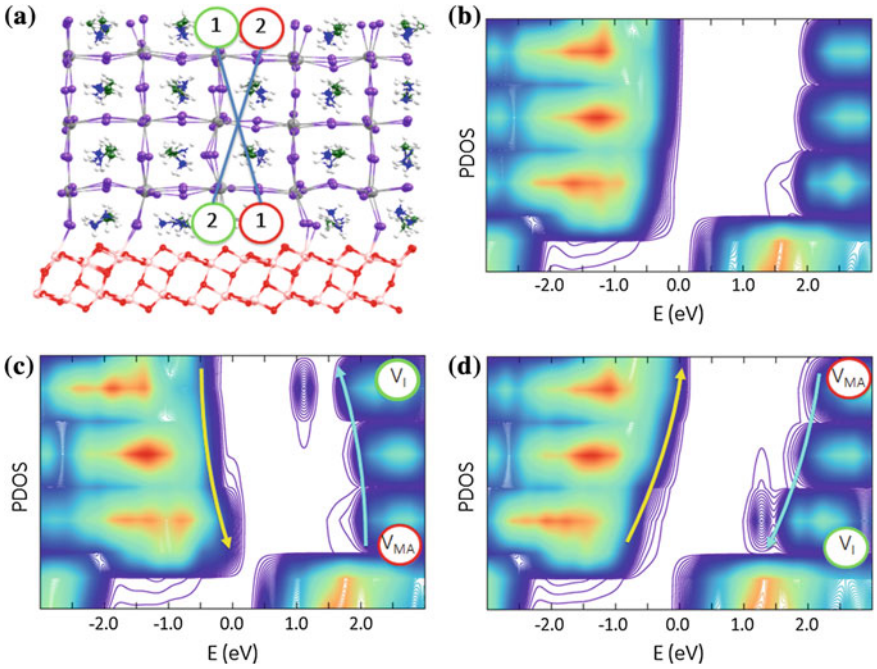

Fig. 9 **a** Perovskite/TiO_2 interface model, where we see V_I (*green circles*) and V_{MA} (*red circles*); Local Density of States (DOS), projected along the direction normal to the perovskite/TiO_2 junction: non-defective model (**b**), and defective models **1** (**c**) and **2** (**d**). *Light-blue* (*yellow*) *arrows* point the evolution of light-absorption generated electrons (holes)

HTL (ETL) is hereafter named **1**. An iodide (MA) vacancy was created at the $MAPbI_3$ surface exposed to vacuum (the $MAPbI_3$ oxide-contacting side—see Fig. 9b). Positive charge migration toward the $CH_3NH_3PbI_3$/titanium oxide contact is further named **2** and is highlighted at Fig. 9c. No geometry relaxation was performed after defects creation in both cases for a direct assessment of the introduction of defects on the electronic structure.

Figure 9 depicts the electronic structure of the two defective models (**1** and **2**). The one of the pristine interface is also present. The partial density of states of titanium oxide and methylammonium lead iodide is displayed together with its local projection along the normal direction to the titanium oxide surface. One can see in the part (b) of the figure that there is an intrusion of perovskite valence band into the titanium oxide bandgap, while the unoccupied states are overlapping with the oxide conduction band. Despite the finite size of the system and the level of theory used for the simulation, [75] we see that the calculations reproduce correctly the energy levels alignment at the titanium oxide/perovskite interface.

Interfacial interactions can be observed by noticing the bending of the perovskite band structure in the vicinity of the titanium oxide surface [55]. If one looks at the influence of defects presence on the electronic structure of a perovskite slab as well as on the interface, we see that the iodide vacancy generates an unoccupied state

below the perovskite conduction band edge (approximately 0.5 eV below, to be relativized due to the overestimation of the perovskite slab bandgap with respect to bulk $CH_3NH_3PbI_3$ material). It therefore appears that there is an overlap between the pervoskite conduction band edge and the state introduced by the iodide vacancy, which is in a good agreement with previous theoretical results [69, 72]. Note that since SOC has been shown to play an important role in the relative positioning of $MAPbI_3$ defective levels, [76] and since spin-orbit coupling is not included in the present calculations, the positioning mentioned above should only be considered on a qualitative basis.

Independently from the level of theory, we see that the presence of positive and negative defects disposed at the opposite sides of the film strongly modifies the perovskite valence/conduction band landscape. For model **2,** one notices the strong directional gradient of unoccupied states close to the titanium oxide substrate due to the presence of iodide vacancy. This actually leads to an increment (a depletion) of unoccupied states at the interface (in the perovskite bulk), which can be seen as a phenomenon boosting interfacial charge injection, also supported by the methylammonium vacancy in **2** which bends the perovskite valence band by introducing an electronic state above the valence band edge (when compared to the pristine valence band edge [69, 72]). Holes migration from the titanium oxide substrate should be facilitated by the slope of the occupied states.

On the other hand, model **1** (Fig. 9c) places iodide vacancies away from the TiO_2 slab and prohibits the electron injection (hole diffusion) into (toward) ETL (HTL), which highly compromises the photovoltaic efficiency of the cell.

Models **1** and **2** have then been modified by considering solely iodide and methylammonium vacancy in the perovskite sides pointing at vacuum and titanium oxide in order to evaluate whether the band edges are overestimated as a consequence of the strong electrostatic interaction existing between positively/negatively charged vacancies. Though the band bending has been reduced by model modification, the valence/conduction band landscape remains quite similar to the unmodified models. Therefore, and beyond the switchable photovoltaic effect, one can consider that the reported results are in good agreement with previous contributions relatively to holes accumulation [77, 78]. Besides, it was suggested that negatively charged defects as iodide interstitials or methylammonium vacancies might be located preferentially in the vicinity of the titanium oxide interface in the absence of an electric field, due to the electron acceptor behavior of undercoordinated titanium atoms. Cationic defects might be more likely to be distributed across the $MAPbI_3$ film. This hypothesis has been reinforced by theoretical results showing a ca. 0.4 eV stabilization energy for model **1** when compared to model **2** using non-relaxed structures. This confirms the role of the substrate in the determination of defects initial concentration close to the selective contacts [79] which is found to be in agreement with recent XPS results pointing the presence of V_{MA} in the surroundings of the titanium oxide/perovskite interface [80].

When computing the stabilization energy of lowest **1** and **2** triplet states, i.e., after the passage of an electron from the perovskite valence band edge to the titanium oxide conduction band (see Fig. 10), one sees that the stability trend is

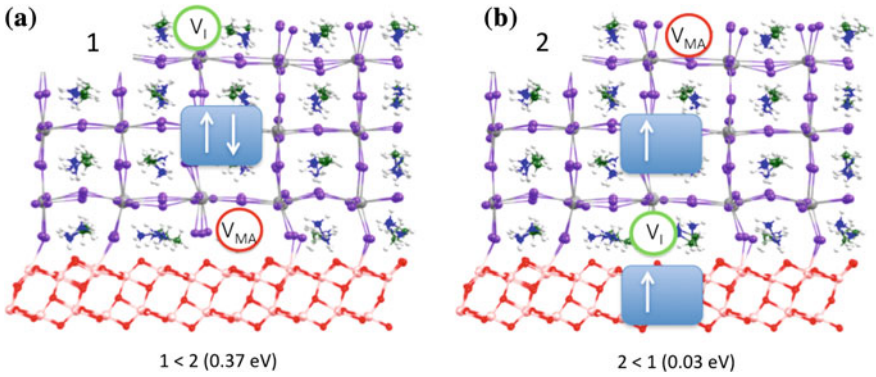

Fig. 10 Iodide and methylammonium vacancies location before (a) and after (b) charge-separation

actually reversed, and that there is no preferential zone for the location of iodide and methymmonium vacancies, which corresponds to an open-circuit cell with a low defect migration driving force. However, the perovskite electronic states landscape was also shown in these results to be quite unchanged by light-induced excitation.

7 The $MAPbI_3$/Water Heterogeneous Interface: Hints on Perovskite Degradation by Water

Among the crucial points characterizing the organohalide perovskite performances we find the perovskite stability. When degradation processes are concerned, one often mentions the presence of moisture, and recent investigations have been devoted to protecting the perovskite layer from the presence of water [81, 82]. Indeed, it has been reported that in the presence of water vapor, hydrated species such as $MAPbI_3{\cdot}H_2O$ or $MA_4PbI_3{\cdot}2H_2O$ can be observed and induce an increase of the cell hysteresis [83]. It has also been shown that PbI_2 can be produced from the irreversible decomposition of $MAPbI_3$ in contact with liquid water, and that at simulated environmental conditions with eighty percent of humidity, a cell aging shows a characteristic perovskite degradation [84]. It was hypothesized that this degradation lead to HI generation [85], which is able to react with the contact electrode silver layer [84]. The water-induced perovskite degradation has also been reported to be a thermodynamically favored process in air [81], and from a mechanistic point of view it was pointed that the first degradation step involves the generation of an intermediate phase containing PbI_6^{4-} as isolated species [82] The degradation process, admittedly accompanied by the generation of this hydrated intermediate phase [86], has also been hypothesized to be assisted by a weakening of the hydrogen bonds connecting the organic to the inorganic parts of MAPbI

through photoexcitation [88]. Such bond weakening favors the perovskite-water interaction, hence perovskite degradation by water.

Considering the impact of humidity on perovskite degradation and cell stability, protection strategies have been suggested, like for example the adjunction of aluminium oxide insulator layer to the device as a way to prevent moisture-caused degradation and TiO_2-spiro-MeOTAD electron recombination [88].

Regarding these issues, attention has been also focused on the role of the hole transporting material [82, 89] (HTM) since the film side on which it is deposited is exposed to the counter electrode. In order to improve the cell resistance to water effects, the replacement of organic HTM by single-wall carbon nanotubes functionalized by a polymer and embedded into an insulator (a polymer matrix) has been suggested [89]. Carbon layers have alternatively been proposed for devices without HTM [90]. Note also that water permeation has been partly suppressed by the implication of vacuum production [92]. On the other hand, it has been reported that ambient air environment (i.e. humid conditions) for the thermal annealing growth of a perovskite precursor film positively impacted the film quality, carrier mobility, grain size and lifetime [93]. It therefore appears that among the various investigations regarding the impact of the presence of water in the vicinity of the perovskite layer, all the conclusions are not strictly convergent and would benefit from a further theoretical insight.

To this end, ab initio molecular dynamics simulations have been performed in order to analyze the nature of the $MAPbI_3/H_2O$ heterointerface, and to characterize the solvation processes responsible for the perovskite degradation and the resulting solvated species [93]. Pending iodine ions nucleophilic substitution has been shown to be a mechanistically possible way for the solvation of MAI-terminated surfaces, supported by methylammonium cation solvation. For its part, the surface terminated by PbI_2 was shown to be less sensitive to the presence of water. This surface, characterized by shorter lead-iodine bonds with respect to the bulk, has therefore been suggested as acting as a protective layer, since no degradation of this surface has been observed within the ten picoseconds timescale of the simulations. Instead, a water molecule insertion into perovskite inorganic framework is observed. $(PbI_2)_n$ vacancy defects generated in PbI_2-poor conditions [94] were shown to lead to a cooperative degradation of the PbI_2-terminated surface, accompanied by the production of solvated species such as $[PbI(H_2O)_5]^+$ or $[PbI_2(H_2O)_6]$. When the perovskite electronic structure is concerned, the impact of hydration is shown to consist in a band gap increase.

Three 2 × 2 slabs have been cut from the bulk $MAPbI_3$ tetragonal crystal structure for simulating the perovskite (001) surfaces (MAI-, PbI_2-terminated and defective surfaces). Those are displayed at Fig. 11. They have been obtained from an optimized bulk structure, for which the methylammonium cations are placed in an isotropic way. Six out of eight PbI units have been removed from the PbI -terminated surface in order to generate a stable defective surface [94]. The a and b cell parameters were taken to be twice the experimental one, i.e. $a = b = 17.71$ Å while $c = 49.67$ Å has been used for the molecular dynamics simulations in water. The water molecules were used to fill the volumes above and below the perovskite

slab, using the experimental liquid water density. Larger water/$MAPbI_3$ ratio has been used for MAI-terminated and PbI_2-defective cases than for PbI_2-terminated simulation, with respectively 284, 235 and 226 water molecules. Similar calculations were performed without water using the same *a* and *b* parameter values and leaving a 10 Å vacuum in the direction perpendicular to the $MAPbI_3$ surface for the sake of comparison. The Car-Parrinello molecular dynamics [95] (CPMD) calculations have been performed using the Quantum Espresso program [96] with the PBE functional [97]. Electron-ion interactions were treated by using a scalar relativistic ultrasoft pseudopotential with electrons from O, N and C 2s, 2p; H 1s; I 5s, 5p; Pb 6s, 6p, 5d shells explicitly included into the calculations. The plane-wave basis set cutoffs were of 25 and 200 Ry respectively for the smooth part of the wavefunctions and for the augmented density. Integration time step of 10 au has been used for the CPMD calculation, for a total simulation time of approximately ten picoseconds. Fictious masses of 1000 au were used for treating the electronic degrees of freedom, while a 5 amu value has been used invariably for all the atomic masses in order to enhance the dynamical sampling. Prior to the use of any thermostat, a thermalization process has been used to reach a 350–400 K temperature by using an initial ions position randomization, and the PWscf code was used, including dispersion contributions [98], for the $4MAPbI_3{\cdot}H_2O$ variable cell geometry optimization, with 50 and 400 Ry cutoffs for the plane wave basis set characterizing the smooth part of the wavefunctions and the augmented density, respectively. The $\Delta G_{form} = E(4MAPbI_3{\cdot}H_2O) - E(4MAPbI_3) - E(H_2O)$ expression has been used for evaluating the formation energy of the hydrated $4MAPbI_3{\cdot}H_2O$ species. Geometry optimization and density of states (DOS) analyses of the hydrated species have been performed using the PWscf code with plane-wave basis sets using cutoff values of 25 and 200 Ry respectively for the smooth part of the wavefunctions and for the augmented density.

The structure of MAI- and PbI_2-terminated slabs were characterized by calculating their radial distribution functions (RDFs). Those were averaged over the dynamics trajectories. Bulk perovskite [13] and bare slabs structures were also compared. It has been shown that the finite size of the models used in the calculations does not significantly alter the crystal structure since bulk RDF properties were seen to be transferred to the bare MAI- and PbI_2- terminated slabs. Note also that the MAI-terminated slabs equatorial Pb-I bond lengths were shown to coincide with those of the bulk, with a 3.21 Å average value, while the average value is 3.19 Å for the PbI_2-terminated surfaces, indicating slightly stronger bonds than in the bulk. This result suggests that such surface may protect the perovskite.

Figure 12 shows the RDFs computed for studying the perovskite/water interfaces for each of the exposed surfaces. Analyzing those RDFs shows us that water molecules have the possibility to bind either to the surface iodine anions (I–H bonds) or to the methylammonium cations (H_{MA}-O bonds) for the MAI-terminated slabs (Fig. 12a), with the typical hydrogen bond length (the average distances are of 2.57 and 1.75 Å respectively). Few short Pb-O bonds were also formed with a 2.75 Å average distance value, which means that water can reach lead by going through the iodine and methylammonium ions network. As far as the PbI -terminated facet

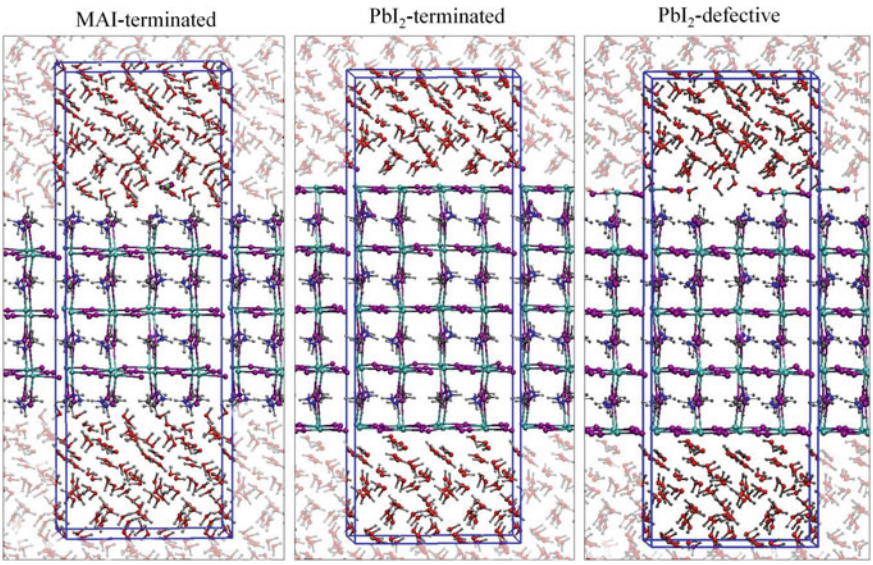

Fig. 11 Structure of the three heterointerfaces (MAI- and PbI_2-terminated, PbI_2-defective slabs) with the simulation cell pointed in blue

is concerned, we see on Fig. 12b that short Pb-O bonds (ca 2.5 Å) can be formed which can be justified from the fact that lead cation is regarded as a borderline hardness acid, which means that it has the possibility to bind soft ligands or hard bases such as the iodine anion from the perovskite or a water molecule respectively. Broad distribution of such pairs has been observed, which suggests a less directional interaction, hence weaker binding between solvent molecules and equatorial iodine atoms in the PbI_2-terminated slab.

One can be interested in describing the dynamical features of the methylammonium lead iodide perovskite, more particularly the methylammonium cation dynamics that can be followed by considering for instance the angle between the ab plane of the perovskite and the MA carbon-nitrogen axis. This angle, written here φ, takes two preferential values ($\pm 30^o$) isotropically distributed in the optimized bulk [13]. When the non-hydrated MAI-terminated surface is concerned, it was shown that for the outermost surface methylammonium cation layers are structured so that the NH groups are pointing toward the surface while the methyl groups are pointing outward, due to stabilizing hydrogen bonds between ammonium and surface iodine atoms. The case of the innermost layer is different: the two peaks at $\varphi = \pm 30^o$ are recovered, indicating that the original MA orientation prevails. If we now focus on the hydrated MAI-terminated surface, we see that the possibility to form interfacial hydrogen bonds with water molecules induces a loss of the preferential orientation described above. Things are less evident for the PbI_2-terminated slab, for which there is a preferential orientation for the ammonium groups that are able to form hydrogen bonds with the surface iodide ions and therefore point toward the surface.

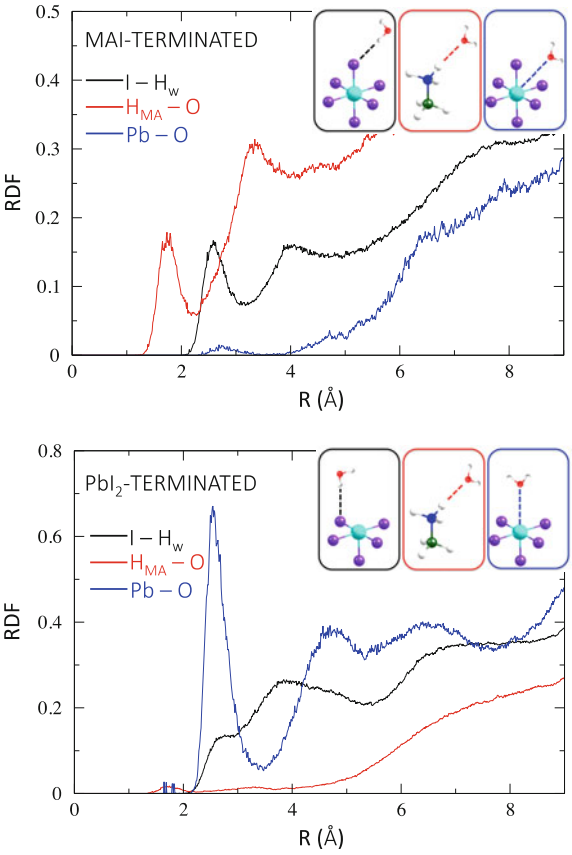

Fig. 12 I–H_w (*black*), H_{MA}–O (*red*), and Pb–O Radial Distribution Functions (RDFs) at the interface between the MAI- (*top panel*) and PbI_2-terminated perovskite slabs (*bottom panel*) and the water layer

This arrangement also impacts the inner layers for which a broad φ angle distribution is observed.

Figure 13 a, b reports the time-evolution of MAI-terminated surface geometrical features. Through the CPMD simulations, observing the Pb-I, Pb-O and Pb-N distances (Fig. 13b) lead to the conclusion that the attack of a water molecule to the surface iodine atoms (Fig. 13a) induces the generation of a seven-coordinated surface lead center, prior to a substitution of iodine by water in the lead coordination sphere, and the release of solvated iodide. The substitution process is characterized by a concerted Pb-I bond weakening (bond length increase) as long as the lead-water bond is formed (decrease of the Pb-water bond length). Moreover, it was shown that due to the iodide release, a vicinal methylammonium cation was detached from the perovskite surface, which prevents the destabilization of the crystal by positive charge accumulation. Through the dynamics, it has been shown that one MAI unit is solvated in 8.5 ps. Though this time scale does not lie within the experimental time scales representative of reaction kinetics, the outcome of these simulations are suggesting that the iodine substitution by water is a fast and

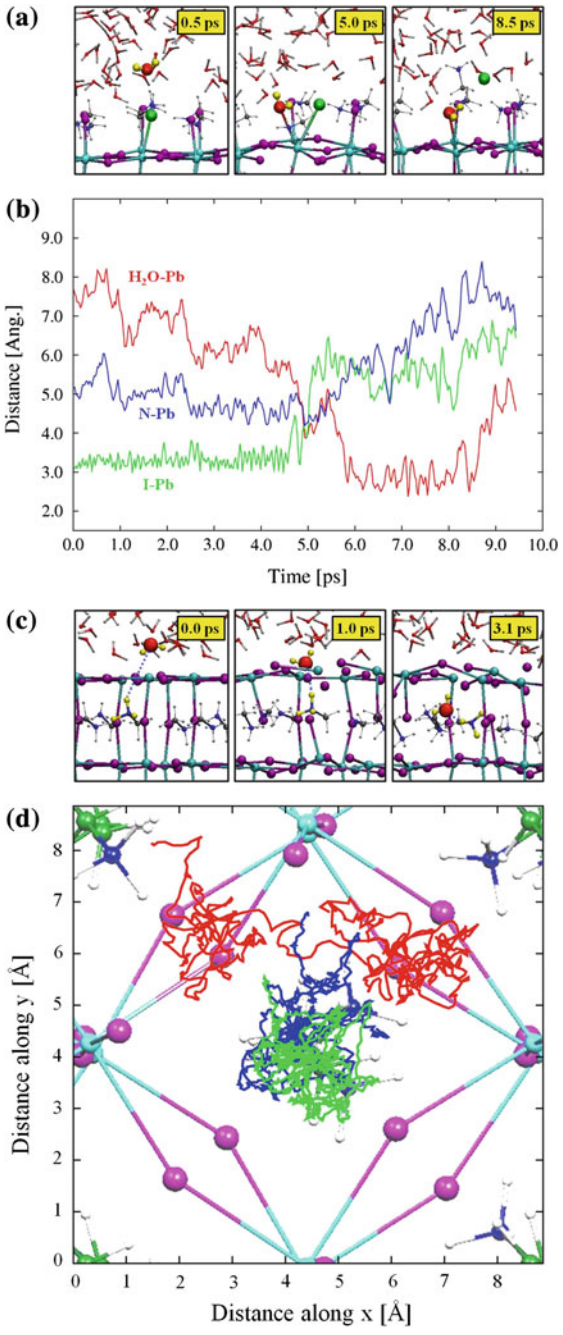

Fig. 13 **a** Nucleophilic substitution of a surface iodide atom by a water molecule in the MAI-terminated $MAPbI_3$ slab, showing the snapshots of the key steps (*top*), and **b** the evolution of the distances (*bottom*) between the water oxygen atom and the lead atom (O–Pb, *red line*), the exiting iodide atom and the lead atom (I–Pb, *green line*), and the MA nitrogen atom and the lead atom (N–Pb, *blue line*). **c** Incorporation of a water molecule to the PbI_2-terminated slab, showing the snapshots of the key steps. **d** Dynamics of the water oxygen atom inside the PbI_2-terminated slab (*red*), along with the trajectories of the MA nitrogen (*blue*) and carbon (*green*) atoms

energetically favorable process, which is in good agreement with previous experimental investigations reporting the MAI solvation as a first step in the perovskite degradation mechanism [99].

Unlike the previous MAI-terminated perovskite slab, the PbI_2-terminated one does not undergo such degradation process despite the existence of strong interactions between water molecules and surface lead atoms. It therefore appears that such PbI_2-terminated surface is more stable with respect to water-induced perovskite decomposition than the MAI-terminated one.

Moreover, one can observe the incorporation of one solvent unit into the methylammonium lead iodide perovskite cavity (Fig. 13c). Indeed, after approximately one picosecond of simulation the water molecule penetrates the cavity by crossing the first PbI layer. A hydrogen bond is further created with a methylammonium cation which, after rotation, traps the water molecule inside of the cavity. This rotation actually follows he path of the water molecule (the ammonium group points toward the water molecule) which was shown to only slightly affect the inorganic scaffold geometry during the simulation. Figure 13d also shows that during the simulation time, the water molecule is sampling two sides of the cavity.

The PbI_2-defective model was further investigated theoretically in order to assess the influence of surface defects and relate them to the relative stability of the water/perovskite heterointerface. To this end, and following previous work [94] indicating that under PbI_2-poor conditions $(PbI_2)_n$ vacancies were stable, six PbI units were removed from the PbI_2-terminated slab, which left two undercoordinated lead atoms on the exposed surface. As reported in Fig. 14, such defective surface can undergo a fast degradation process. Indeed, we see that the two undercoordinated lead atoms can rapidly desorb from the surface and migrate as solvated species. In Fig. 14a we see that one of the lead atoms was initially bonded one water molecule and to the MAPbI surface through four iodine atoms while the second lead atom was shown to bind three iodine atoms and two interfacial water molecules (Fig. 14b). Both have in common that after departing from the surface, they form solvated complexes, respectively $[PbI_2(H_2O)_4]$ and $[PbI(H_2O)_5]$ as displayed in Fig. 14c in which the coordination number of these two undercoordinated lead atoms is reproduced through the dynamics trajectory. In summary, these results show that imperfections at the perovskite surface may play a crucial role in the degradation process of MAPbI perovskite. The importance of the preparation of crystals and thin films without defect is therefore pointed as a relevant element for further considering the elaboration of stable devices based on perovskite material.

The interaction between MAI- and PbI-terminated slabs and a monolayer of eight H_2O molecules has been investigated in order to assess the influence of surface hydration on the slabs electronic structure. The local DOS is displayed in Fig. 15 for the considered perovskite slabs. Note that the MA cations arrangement induces the absence of any dipole across the slabs, which is desired for examinating the surface termination and hydration effects solely. Note also that the number of water molecules has been chosen so as to correspond to a saturation of the undercoordinated sites of all the surface. A strong driving force has been reported

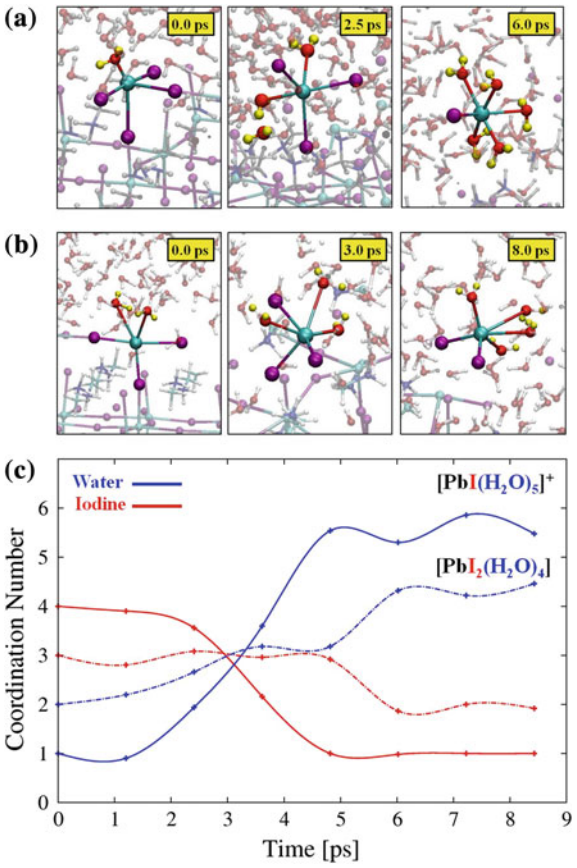

Fig. 14 Representative geometrical structures of the formation of **a** $[PbI_2(H_2O)_4]$ and **b** $[PbI(H_2O)_5]^+$ complexes. **c** Evolution of the Pb–I (*red*) and Pb–H_2O (*blue*) coordination numbers for the formation of $[PbI_2(H_2O)_4]$ (*dot-dashed lines*) and $[PbI(H_2O)_5]^+$ (*solid lines*) species

for this surface hydration, with formation energies being respectively of −0.49 and −0.44 eV for the MAI- and PbI_2-terminated hydrated slabs.

Interestingly, it was also noticed that using a scalar relativistic DFT protocol allows one to accurately reproduce the band-gap of MAPbI [32,33], but in a fortuitous way. Indeed, there exists a possible error cancellation [39] between spin-orbit coupling and post-DFT correlation which respectively reduces and augments the gap. Local perovskite structure, and more particularly the PbI octahedra tilting [54], was shown to be responsible for the influence of spin-orbit coupling, though this contribution is quasi constant across the slabs. It is therefore expected that the computational protocol employed is able to qualitatively reproduce the electronic structure variations characterizing the bare and hydrated surfaces.

It was observed that the bare MAI-terminated surface band-gap gets sharper when moving inward through the perovskite layers, which can be explained by the stabilization of the external valence band edge when compared to the inner one (see Fig. 15a) and the interaction between methylammonium cations and the external

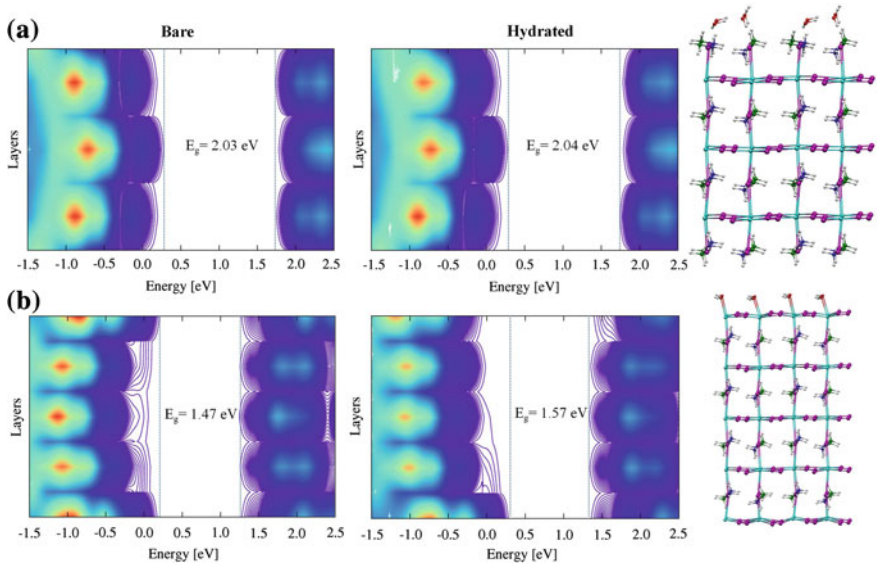

Fig. 15 Isodensityplot of the local density of states across the various perovskite layers found in the [001] direction, i.e., along the crystal *c* axis, in the bandgap region for **a** the bare and hydrated MAI-terminated; and **b** the PbI_2-terminated perovskite slabs. Also reported are the global bandgap values. The vertical dashed lines represent the valence and conduction bands for an isodensity value of 1 state/eV

iodine atoms, which lowers their energy levels. Conversely, for the PbI_2-terminated surface, the band-gap broadens when moving inward through the perovskite layers because of the undercoordinated lead atoms present at the surface. It has also been noticed that while for the PbI -terminated slab the valence band edge is located at the perovskite surface, which may ultimately lead to a trapping of the photogenerated holes, only a limited effect of MAPbI has been suggested to occur for the MAI-terminated slab, due to the fact that no surface states intrudes into the perovskite gap. Hydration effect has been shown to produce quasi no effect on the MAI-terminated model, as hydrogen bonds are mostly responsible for the water/perovskite interfacial interactions. As far as the PbI_2-terminated model is concerned, it was shown that the valence band edge is stabilized in the hydrated interfacial region with respect to the bare surface, with a water-induced valence band down-shift, which was explained by the restoration of the surface lead atoms coordination sphere. This shift is however not compensated by a conduction band shift, which leads to a local band-gap increase of ca. 0.3 eV.

In the continuity of the results related to the incorporation of one H_2O molecule into the PbI_2-terminated slab, the effect on the electronic structure of the inclusion of one water molecule into the bulk perovskite was also investigated, using a bare and a mono-hydrated 48-atom tetragonal unit cell. Geometry relaxation was performed on these two systems and showed that water insertion into the perovskite

cavity is thermodynamically favored by ca. 0.45 eV which indicates the possible spontaneous formation of the hydrated phase, as resulting from the CPDM simulation. Hydration also impacts the band-gap energy value, increasing from 1.45 eV for the bare system to 1.50 eV for the hydrated one. Note also that only a slight cell volume increase was reported (1.3 %) due to the hydration, and that the overall tetragonal shape was preserved, with a c/a ratio moving from 1.48 for the bare MAPbI to 1.47 for the hydrated system. These results indicate the possible existence of a new intermediate hydrated phase characterized by a 4:1 $MAPbI_3$:H_2O ratio (different from the 1:1 and the 1:2 ratio previously reported in the literature [83]) preserving the overall structure and electronic features apart for the slight band-gap modifications. Indeed, it has then been demonstrated that the methylammonium lead iodide perovskite electronic properties might be modulated by exposing the perovskite to water, while the structural parameters are left unaltered by such treatment.

It can therefore be concluded that such results are of importance for understanding the effect of the environment on the stability of these $MAPbI_3$ perovskites as the water-induced degradation of these systems are considered as the main perovskite alteration channel.

This computational investigation aimed at understanding these water/perovskite interactions at the atomic scale, by considering MAI- and PbI_2-terminated surfaces characterizing the most probable systems grown under MAI-rich and poor conditions. The interaction between water and lead sites in the MAI-terminated surfaces drives the rapid solvation of these facets and the release of solvated iodine atoms following a nucleophilic substitution of iodine by water and the desorption of methylammonium cations, resulting in the net solvation of a methylammonium iodide ion pair, which was in good agreement with the previously reported experimental conclusions. PbI_2-terminated slabs did not exhibit such behavior when in contact with water molecules, indicating the possible action of such surface as a protective layer for the perovskite against water-caused degradation. However, water percolation has been observed for this type of slab, suggesting the existence of a novel form of hydrated bulk phase preserving geometrical parameters unaltered. On the other hand, PbI -defective systems were showed to be more susceptible to undergo water-induced degradation.

The MAI- and PbI_2-terminated systems hydration was computationally shown to be exergonic, and hydration was shown to have a non-significant impact on the electronic strucutre of the MAI-terminated system, given that the adsorption is mostly driven by hydrogen bond formation between water and the methylammonium cations. Conversely, it has been shown that the valence band edge of the PbI_2-terminated slabs is stabilized in the interfacial zone in the presence of a water monolayer. A band-gap increase of approximately 0.3 eV was also observed in such case. The impact on the perovskite electronic structure of water incorporation into bulk MAPbI has also been studied using a 4:1 perovskite:water ratio. It was shown that such process causes the increase of the perovskite band-gap from 1.45 to 1.50 eV, while the structural parameters remained unaltered, with only a one-percent volume increase, which indicates that the incorporation of one water molecule

could possibly occur without being detected by usual structural characterization techniques. Based on these novel knowledge, it is now possible to imagine new interfacial alterations and to generate more stable perovskite architectures, which in turn could play a role in new performant solar cells devices.

References

1. Bisquert, J.: The swift surge of perovskite photovoltaics. J. Phys. Chem. Lett. **4**, 2597–2598 (2013)
2. Salau, A.M.: Fundamental absorption edge in PbI2:KI alloys. Solar Energy Mater. **2**, 327–332 (1980)
3. Gao, P., Gratzel, M., Nazeeruddin, M.K.: Organohalide lead perovskites for photovoltaic applications. Energy Environ. Sci. **7**, 2448–2463 (2014)
4. Kojima, A., Teshima, K., Shirai, Y., Miyasaka, T.: Organometal halide perovskites as visible-light sensitizers for photovoltaic cells. J. Am. Chem. Soc. **131**, 6050–6051 (2009)
5. Im, J.-H., Lee, C.-R., Lee, J.-W., Park, S.-W., Park, N.-G.: 6.5 % efficient perovskite quantum-dot-sensitized solar cell. Nanoscale **3**, 4088–4093
6. Kim, H.-S., Lee, C.-R., Im, J.-H., Lee, K.-B., Moehl, T., Marchioro, A., Moon, S.-J., Humphry-Baker, R., Yum, J.-H., Moser, J.E., Grätzel, M., Park, N.-G.: Lead Iodide perovskite sensitized all-solid-state submicron thin film mesoscopic solar cell with efficiency exceeding 9 %. Sci. Rep. **2**, 591 (2012)
7. Lee, M.M., Teuscher, J.l., Miyasaka, T., Murakami, T.N., Snaith, H.J.: Efficient hybrid solar cells based on meso-superstructured organometal halide perovskites. Science **338**, 643–647
8. Heo, J.H., Im, S.H., Noh, J.H., Mandal, T.N., Lim, C.-S., Chang, J.A., Lee, Y.H., Kim, H.-J., Sarkar, A., NazeeruddinMd, K., Gratzel, M., Seok, S.I.: Efficient inorganic-organic hybrid heterojunction solar cells containing perovskite compound and polymeric hole conductors. Nat. Photon. **7**, 486–491 (2013)
9. Burschka, J., Pellet, N., Moon, S.-J., Humphry-Baker, R., Gao, P., Nazeeruddin, M.K., Gratzel, M.: Sequential deposition as a route to high-performance perovskite-sensitized solar cells. Nature **499**, 316–319 (2013)
10. Liu, M., Johnston, M.B., Snaith, H.J.: Efficient planar heterojunction perovskite solar cells by vapour deposition. Nature **501**, 395–398 (2013)
11. Zhou, H., Chen, Q., Li, G., Luo, S., Song, T.-B., Duan, H.-S., Hong, Z., You, J., Liu, Y., Yang, Y.: Interface engineering of highly efficient perovskite solar cells. Science **345**, 542–546 (2014)
12. Green, M.A., Ho-Baillie, A., Snaith, H.J.: The emergence of perovskite solar cells. Nat. Photon. **8**, 506–514 (2014)
13. Quarti, C., Mosconi, E., De Angelis, F.: Interplay of orientational order and electronic structure in methylammonium lead Iodide: implications for solar cell operation. Chem. Mater. **26**, 6557–6569 (2014)
14. Quarti, C., Grancini, G., Mosconi, E., Bruno, P., Ball, J.M., Lee, M.M., Snaith, H.J., Petrozza, A., Angelis, F.D.: The Raman spectrum of the $CH_3NH_3PbI_3$ hybrid perovskite: interplay of theory and experiment. J. Phys. Chem. Lett. **5**, 279–284 (2013)
15. Mosconi, E., Quarti, C., Ivanovska, T., Ruani, G., De Angelis, F.: Structural and electronic properties of organo-halide lead perovskites: a combined IR-spectroscopy and ab initio molecular dynamics investigation. Phys. Chem. Chem. Phys. **16**, 16137–16144 (2014)
16. Wehrenfennig, C., Eperon, G.E., Johnston, M.B., Snaith, H.J., Herz, L.M.: High charge carrier mobilities and lifetimes in organo lead trihalide perovskites. Adv. Mater. **26**, 1584–1589 (2014)

17. Stranks, S.D., Eperon, G.E., Grancini, G., Menelaou, C., Alcocer, M.J.P., Leijtens, T., Herz, L.M., Petrozza, A., Snaith, H.J.: Electron-hole diffusion lengths exceeding 1 micrometer in an organometal trihalide perovskite absorber. Science **342**, 341–344 (2013)
18. D'Innocenzo, V., Grancini, G., Alcocer, M.J.P., Kandada, A.R.S., Stranks, S.D., Lee, M.M., Lanzani, G., Snaith, H.J., Petrozza, A.: Excitons versus free charges in organo-lead tri-halide perovskites. Nat. Commun. **5**, 3586 (2014)
19. Edri, E., Kirmayer, S., Henning, A., Mukhopadhyay, S., Gartsman, K., Rosenwaks, Y., Hodes, G., Cahen, D.: Why lead methylammonium tri-iodide perovskite-based solar cells require a mesoporous electron transporting scaffold (but not necessarily a hole conductor). Nano Lett. **14**, 1000–1004 (2014)
20. Edri, E., Kirmayer, S., Mukhopadhyay, S., Gartsman, K., Hodes, G., Cahen, D.: Elucidating the charge carrier separation and working mechanism of CH3NH3PbI3–xClx perovskite solar cells. Nat. Commun. **5**, 3461 (2014)
21. Lv, H., Gao, H., Yang, Y., Liu, L.: Density functional theory (DFT) investigation on the structure and electronic properties of the cubic perovskite $PbTiO_3$. App. Catal. A **404**, 54–58 (2011)
22. Borriello, I., Cantele, G., Ninno, D.: Ab initio investigation of hybrid organic-inorganic perovskites based on tin halides. Phys. Rev. B **77**, 235214 (2008)
23. Castelli, I.E., Olsen, T., Datta, S., Landis, D.D., Dahl, S., Thygesen, K.S., Jacobsen, K.W.: Computational screening of perovskite metal oxides for optimal solar light capture. Energy Environ. Sci. **5**, 5814–5819 (2012)
24. Hedin, L.: New method for calculating the one-particle green's function with application to the electron-gas problem. Phys. Rev. **139**, A796–A823 (1965)
25. Hybertsen, M.S., Louie, S.G.: Electron correlation in semiconductors and insulators: band gaps and quasiparticle energies. Phys. Rev. B **34**, 5390–5413 (1986)
26. Umari, P., Qian, X., Marzari, N., Stenuit, G., Giacomazzi, L., Baroni, S.: Accelerating GW calculations with optimal polarizability basis. Phys. Status Solidi B **248**, 527–536 (2011)
27. Di Valentin, C., Pacchioni, G., Selloni, A.: Electronic structure of defect states in hydroxylated and reduced rutile TiO_2 (110) surfaces. Phys. Rev. Lett. **97**, 166803 (2006)
28. Berger, R.F., Neaton, J.B.: Computational design of low-band-gap double perovskites. Phys. Rev. B **86**, 165211 (2012)
29. Umebayashi, T., Asai, K., Kondo, T., Nakao, A.: Electronic structures of lead iodide based low-dimensional crystals. Phys. Rev. B **67**, 155405 (2003)
30. Baikie, T., Fang, Y., Kadro, J.M., Schreyer, M., Wei, F., Mhaisalkar, S.G., Grätzel, M., White, T.J.: Synthesis and crystal chemistry of the hybrid perovskite $(CH_3NH_3)PbI_3$ for solid-state sensitised solar cell applications. J. Mater. Chem. A **1**, 5628–5641 (2013)
31. Takahashi, Y., Obara, R., Lin, Z.-Z., Takahashi, Y., Naito, T., Inabe, T., Ishibashi, S., Terakura, K.: Charge-transport in tin-iodide perovskite $CH_3NH_3SnI_3$: origin of high conductivity. Dalton Trans. **40**, 5563–5568 (2011)
32. Mosconi, E., Amat, A., Nazeeruddin, M.K., Grätzel, M., De Angelis, F.: First-principles modeling of mixed halide organometal perovskites for photovoltaic applications. J. Phys. Chem. C **117**, 13902–13913 (2013)
33. Even, J., Pedesseau, L., Jancu, J.-M., Katan, C.: Importance of spin-orbit coupling in hybrid organic/inorganic perovskites for photovoltaic applications. J. Phys. Chem. Lett. **4**, 2999–3005 (2013)
34. Stoumpos, C.C., Malliakas, C.D., Kanatzidis, M.G.: Semiconducting Tin and Lead Iodide perovskites with organic cations: phase transitions, high mobilities, and near-infrared photoluminescent properties. Inorg. Chem. **52**, 9019–9038 (2013)
35. Papavassiliou, G.C., Koutselas, I.B.: Structural, optical and related properties of some natural three- and lower-dimensional semiconductor systems. Synthetic Met. **71**, 1713–1714 (1995)
36. Chung, I., Lee, B., He, J., Chang, R.P.H., Kanatzidis, M.G.: All-solid-state dye-sensitized solar cells with high efficiency. Nature **485**, 486–489 (2012)

37. Etgar, L., Gao, P., Xue, Z., Peng, Q., Chandiran, A.K., Liu, B., Nazeeruddin, M.K., Grätzel, M.: Mesoscopic $CH_3NH_3PbI_3/TiO_2$ heterojunction solar cells. J. Am. Chem. Soc. **134**, 17396–17399 (2012)
38. Sakuma, R., Friedrich, C., Miyake, T., Blügel, S., Aryasetiawan, F.: GW calculations including spin-orbit coupling: application to Hg chalcogenides. Phys. Rev. B **84**, 085144 (2011)
39. Umari, P., Mosconi, E., De Angelis, F.: Relativistic GW calculations on $CH_3NH_3PbI_3$ and $CH_3NH_3SnI_3$ perovskites for solar cell applications. Sci. Rep. **4**, 4467 (2014)
40. Lee, M.M., Teuscher, J., Miyasaka, T., Murakami, T.N., Snaith, H.J.: Efficient hybrid solar cells based on meso-superstructured organometal halide perovskites. Science **338**, 643–647 (2012)
41. Colella, S., Mosconi, E., Fedeli, P., Listorti, A., Gazza, F., Orlandi, F., Ferro, P., Besagni, T., Rizzo, A., Calestani, G., Gigli, G., De Angelis, F., Mosca, R.: $MAPbI_{3-x}Cl_x$ mixed halide perovskite for hybrid solar cells: the role of chloride as dopant on the transport and structural properties. Chem. Mater. **25**, 4613–4618 (2013)
42. Yamada, K., Nakada, K., Takeuchi, Y., Nawa, K., Yamane, Y.: Tunable perovskite semiconductor $CH_3NH_3SnX_3$ (X: Cl, Br, or I) characterized by X-ray and DTA. Bull. Chem. Soc. Jpn. **84**, 926–932 (2011)
43. Zhao, Y., Zhu, K.: CH3NH3Cl-assisted one-step solution growth of CH3NH3PbI3: structure, charge-carrier dynamics, and photovoltaic properties of perovskite solar cells. J. Phys. Chem. C **118**, 9412–9418 (2014)
44. Edri, E., Kirmayer, S., Kulbak, M., Hodes, G., Cahen, D.: Chloride inclusion and hole transport material doping to improve methyl ammonium lead bromide perovskite-based high open-circuit voltage solar cells. J. Phys. Chem. Lett. **5**, 429–433 (2014)
45. Conings, B., Baeten, L., De Dobbelaere, C., D'Haen, J., Manca, J., Boyen, H.-G.: Perovskite-based hybrid solar cells exceeding 10 % efficiency with high reproducibility using a thin film sandwich approach. Adv. Mater. **26**, 2041–2046 (2013)
46. Kim, H.-B., Choi, H., Jeong, J., Kim, S., Walker, B., Song, S., Kim, J.Y.: Mixed solvents for the optimization of morphology in solution-processed, inverted-type perovskite/fullerene hybrid solar cells. Nanoscale
47. Chen, Q., Zhou, H., Hong, Z., Luo, S., Duan, H.-S., Wang, H.-H., Liu, Y., Li, G., Yang, Y.: Planar heterojunction perovskite solar cells via vapor-assisted solution process. J. Am. Chem. Soc. **136**, 622–625 (2013)
48. Qiu, J., Qiu, Y., Yan, K., Zhong, M., Mu, C., Yan, H., Yang, S.: All-solid-state hybrid solar cells based on a new organometal halide perovskite sensitizer and one-dimensional TiO_2 nanowire arrays. Nanoscale **5**, 3245–3248 (2013)
49. Liang, P.-W., Liao, C.-Y., Chueh, C.-C., Zuo, F., Williams, S.T., Xin, X.-K., Lin, J., Jen, A.K. Y.: Additive enhanced crystallization of solution-processed perovskite for highly efficient planar-heterojunction solar cells. Adv. Mater. **26**, 3748–3754 (2014)
50. Eperon, G.E., Burlakov, V.M., Docampo, P., Goriely, A., Snaith, H.J.: Morphological control for high performance, solution-processed planar heterojunction perovskite solar cells. Adv. Funct. Mater. **24**, 151–157 (2014)
51. Noh, J.H., Im, S.H., Heo, J.H., Mandal, T.N., Seok, S.I.: Chemical management for colorful, efficient, and stable inorganic-organic hybrid nanostructured solar cells. Nano Lett. **13**, 1764–1769 (2013)
52. Kim, H.-S., Mora-Sero, I., Gonzalez-Pedro, V., Fabregat-Santiago, F., Juarez-Perez, E.J., Park, N.-G., Bisquert, J.: Mechanism of carrier accumulation in perovskite thin-absorber solar cells. Nat. Commun. **4** (2013)
53. Poglitsch, A., Weber, D.: Dynamic disorder in methylammoniumtrihalogenoplumbates (II) observed by millimeter-wave spectroscopy. J. Chem. Phys. **87**, 6373–6378 (1987)
54. Amat, A., Mosconi, E., Ronca, E., Quarti, C., Umari, P., Nazeeruddin, M.K., Grätzel, M., De Angelis, F.: Cation-induced band-gap tuning in organohalide perovskites: interplay of spin-orbit coupling and octahedra tilting. Nano Lett. **14**, 3608–3616 (2014)

55. Roiati, V., Mosconi, E., Listorti, A., Colella, S., Gigli, G., De Angelis, F.: Stark effect in perovskite/TiO2 solar cells: evidence of local interfacial order. Nano Lett. **14**, 2168–2174 (2014)
56. Mitzi, D.B.: Solution-processed inorganic semiconductors. J. Mater. Chem. **14**, 2355–2365 (2004)
57. Mosconi, E., Ronca, E., De Angelis, F.: First-principles investigation of the TiO2/organohalide perovskites interface: the role of interfacial chlorine. J. Phys. Chem. Lett. **5**, 2619–2625 (2014)
58. Feng, H.-J., Paudel, T.R., Tsymbal, E.Y., Zeng, X.C.: Tunable optical properties and charge separation in CH3NH3SnxPb1–xI3/TiO2-based planar perovskites cells. J. Am. Chem. Soc. **137**, 8227–8236 (2015)
59. Lindblad, R., Bi, D., Park, B.-W., Oscarsson, J., Gorgoi, M., Siegbahn, H., Odelius, M., Johansson, E.M.J., Rensmo, H.: Electronic structure of TiO2/CH3NH3PbI3 perovskite solar cell interfaces. J. Phys. Chem. Lett. **5**, 648–653 (2014)
60. Miller, E.M., Zhao, Y., Mercado, C.C., Saha, S.K., Luther, J.M., Zhu, K., Stevanovic, V., Perkins, C.L., van de Lagemaat, J.: Substrate-controlled band positions in CH3NH3PbI3 perovskite films. Phys. Chem. Chem. Phys. **16**, 22122–22130 (2014)
61. Schulz, P., Edri, E., Kirmayer, S., Hodes, G., Cahen, D., Kahn, A.: Interface energetics in organo-metal halide perovskite-based photovoltaic cells. Energy Environ. Sci. **7**, 1377–1381 (2014)
62. Baena, J.P.C., Steier, L., Tress, W., Saliba, M., Neutzner, S., Matsui, T., Giordano, F., Jacobsson, T.J., Kandada, A.R.S., Zakeeruddin, S. M., Petrozza, A., Abate, A., Nazeeruddin, M.K., Gratzel, M., Hagfeldt, A.: Highly efficient planar perovskite solar cells through band alignment engineering. Energy Environ. Sci. **8**, 2928–2934 (2015)
63. Tress, W., Marinova, N., Moehl, T., Zakeeruddin, S.M., Nazeeruddin, M.K., Grätzel, M.: Understanding the rate-dependent J–V hysteresis, slow time component, and aging in CH3NH3PbI3 perovskite solar cells: the role of a compensated electric field. Energy Environ. Sci. **8**, 995–1004 (2015)
64. Roldan-Carmona, C., Gratia, P., Zimmermann, I., Grancini, G., Gao, P., Graetzel, M., Nazeeruddin, M.K.: High efficiency methylammonium lead triiodide perovskite solar cells: the relevance of non-stoichiometric precursors. Energy Environ. Sci. **8**, 3550–3556 (2015)
65. Mosconi, E., Grancini, G., Roldan-Carmona, C., Gratia, P., Zimmermann, I., Nazeeruddin, M. K., De Angelis, F.: Enhanced TiO2/MAPbI3 electronic coupling by interface modification with PbI2. Chem. Mater. (submitted to, 2016)
66. Yang, J., Siempelkamp, B.D., Mosconi, E., De Angelis, F., Kelly, T.L.: Origin of the thermal instability in CH3NH3PbI3 thin films deposited on ZnO. Chem, Mater (2015)
67. Azpiroz, J.M., Mosconi, E., Bisquert, J., De Angelis, F.: Defect migration in methylammonium lead iodide and its role in perovskite solar cell operation. Energy Environ. Sci. **8**, 2118–2127 (2015)
68. Agiorgousis, M.L., Sun, Y.-Y., Zeng, H., Zhang, S.: Strong covalency-induced recombination centers in perovskite solar cell material CH3NH3PbI3. J. Am. Chem. Soc. **136**, 14570–14575 (2014)
69. Buin, A., Pietsch, P., Xu, J., Voznyy, O., Ip, A.H., Comin, R., Sargent, E.H.: Materials processing routes to trap-free halide perovskites. Nano Lett. **14**, 6281–6286 (2014)
70. Du, M.H.: Efficient carrier transport in halide perovskites: theoretical perspectives. J. Mater. Chem. A **2**, 9091–9098 (2014)
71. Walsh, A., Scanlon, D.O., Chen, S., Gong, X.G., Wei, S.-H.: Self-regulation mechanism for charged point defects in hybrid halide perovskites. Angew. Chem. Int. Ed. **53**, 1–5 (2014)
72. Yin, W.-J., Shi, T., Yan, Y.: Unusual defect physics in CH3NH3PbI3 perovskite solar cell absorber. Appl. Phys. Lett. **104**, 063903 (2014)
73. Almora, O., Zarazua, I., Mas-Marza, E., Mora-Sero, I., Bisquert, J., Garcia-Belmonte, G.: Capacitive dark currents, hysteresis, and electrode polarization in lead halide perovskite solar cells. J. Phys. Chem. Lett. **6**, 1645–1652 (2015)

74. Xiao, Z., Yuan, Y., Shao, Y., Wang, Q., Dong, Q., Bi, C., Sharma, P., Gruverman, A., Huang, J.: Giant switchable photovoltaic effect in organometal trihalide perovskite devices. Nat. Mater. **14**, 193–198 (2014)
75. Mosconi, E., Amat, A., Nazeeruddin, K., Grätzel, M., De Angelis, F.: First-principles modeling of mixed halide organometal perovskites for photovoltaic applications. J. Phys. Chem. C **117** (2013)
76. Du, M.-H.: Density functional calculations of native defects in CH3NH3PbI3: effects of spin-orbit coupling and self-interaction error. J. Phys. Chem. Lett. **6**, 1461–1466 (2015)
77. Bergmann, V.W., Weber, S.A.L., Ramos, F.J., Nazeeruddin, M.K., Grätzel, M., Li, D., Domanski, A.L., Lieberwirth, I., Ahmad, S.: Real-space observation of unbalanced charge distribution inside a perovskite-sensitized solar cell. Nat. Commun. 1–9 (2014)
78. Edri, E., Kirmayer, S., Mukhopadhyay, S., Gartsman, K., Hodes, G., Cahen, D.: Elucidating the charge carrier separation and working mechanism of CH3NH3PbI3–xClx perovskite solar cells. Nat. Commun. 1–8 (2014)
79. Snaith, H.J., Abate, A., Ball, J.M., Eperon, G.E., Leijtens, T., Noel, N.K., Stranks, S.D., Wang, J.T.-W., Wojciechowski, K., Zhang, W.: Anomalous hysteresis in perovskite solar cells. J. Phys. Chem. Lett. **5**, 1511–1515 (2014)
80. Xing, G., Wu, B., Chen, S., Chua, J., Yantara, N., Mhaisalkar, S., Mathews, N., Sum, T.C.: Interfacial electron transfer barrier at compact TiO2/CH3NH3PbI3 heterojunction. Small **11**, 3606–3613 (2015)
81. Niu, G., Li, W., Meng, F., Wang, L., Dong, H., Qiu, Y.: Study on the stability of CH3NH3PbI3 films and the effect of post-modification by aluminum oxide in all-solid-state hybrid solar cells. J. Mater. Chem. A **2**, 705–710 (2014)
82. Yang, J., Siempelkamp, B.D., Liu, D., Kelly, T.L.: Investigation of CH3NH3PbI3 degradation rates and mechanisms in controlled humidity environments using in situ techniques. ACS Nano **9**, 1955–1963 (2015)
83. Leguy, A., Hu, Y., Campoy-Quiles, M., Alonso, M.I., Weber, O.J., Azarhoosh, P., van Schilfgaarde, M., Weller, M.T., Bein, T., Nelson, J., Docampo, P., Barnes, P.R.F.: The reversible hydration of CH3 NH3PbI3 in films, single crystals and solar cells. Chem. Mater. **27**, 3397–3407 (2015)
84. Han, Y., Meyer, S., Dkhissi, Y., Weber, K., Pringle, J.M., Bach, U., Spiccia, L., Cheng, Y.-B.: Degradation observations of encapsulated planar CH3NH3PbI3 perovskite solar cells at high temperatures and humidity. J. Mater. Chem. A **3**, 8139–8147 (2015)
85. Frost, J.M., Butler, K.T., Brivio, F., Hendon, C.H., van Schilfgaarde, M., Walsh, A.: Atomistic origins of high-performance in hybrid halide perovskite solar cells. Nano Lett. **14**, 2584–2590 (2014)
86. Christians, J.A., Miranda Herrera, P.A., Kamat, P.V.: Transformation of the excited state and photovoltaic efficiency of CH3NH3PbI3 perovskite upon controlled exposure to humidified air. J. Am. Chem. Soc. **137**, 1530–1538 (2015)
87. Gottesman, R., Haltzi, E., Gouda, L., Tirosh, S., Bouhadana, Y., Zaban, A., Mosconi, E., De Angelis, F.: Extremely slow photoconductivity response of CH3NH3PbI3 perovskites suggesting structural changes under working conditions. J. Phys. Chem. Lett. **5**, 2662–2669 (2014)
88. Dong, X., Fang, X., Lv, M., Ling, B., Zhang, S., Ding, J., Yuan, N.: Improvement of the humidity stability of organic-inorganic perovskite solar cells using ultrathin Al2O3 layers prepared by atomic layer deposition. J. Mater. Chem. A **3**, 5360–5367 (2015)
89. Habisreutinger, S.N., Leijtens, T., Eperon, G.E., Stranks, S.D., Nicholas, R.J., Snaith, H.J.: Carbon nanotube/polymer composites as a highly stable hole collection layer in perovskite solar cells. Nano Lett. **14**, 5561–5568 (2014)
90. Mei, A., Li, X., Liu, L., Ku, Z., Liu, T., Rong, Y., Xu, M., Hu, M., Chen, J., Yang, Y., Grätzel, M., Han, H.: A hole-conductor–free, fully printable mesoscopic perovskite solar cell with high stability. Science **345**, 295–298 (2014)

91. Xie, F.X., Zhang, D., Su, H., Ren, X., Wong, K.S., Grätzel, M., Choy, W.C.H.: Vacuum-assisted thermal annealing of CH3NH3PbI3 for highly stable and efficient perovskite solar cells. ACS Nano **9**, 639–646 (2015)
92. You, J., Yang, Y., Hong, Z., Song, T.-B., Meng, L., Liu, Y., Jiang, C., Zhou, H., Chang, W.-H., Li, G.: Moisture assisted perovskite film growth for high performance solar cells. Appl. Phys. Lett. **105**, 183902 (2014)
93. Mosconi, E., Azpiroz, J.M., De Angelis, F.: Ab Initio molecular dynamics simulations of methylammonium lead iodide perovskite degradation by water. Chem. Mater. **27**, 4885–4892 (2015)
94. Haruyama, J., Sodeyama, K., Han, L., Tateyama, Y.: Termination dependence of tetragonal CH3NH3PbI3 surfaces for perovskite solar cells. J. Phys. Chem. Lett. **5**, 2903–2909 (2014)
95. Car, R., Parrinello, M.: Unified Approach for molecular dynamics and density-functional theory. Phys. Rev. Lett. **55**, 2471–2474 (1985)
96. Giannozzi, P., Baroni, S., Bonini, N., Calandra, M., Car, R., Cavazzoni, C., Ceresoli, D., Guido, L.C., Cococcioni, M., Dabo, I., Corso, A.D., Gironcoli, S.D., Fabris, S., Fratesi, G., Gebauer, R., Gerstmann, U., Gougoussis, C., Kokalj, A., Lazzeri, M., Martin-Samos, L., Marzari, N., Mauri, F., Mazzarello, R., Paolini, S., Pasquarello, A., Paulatto, L., Sbraccia, C., Scandolo, S., Sclauzero, G., Seitsonen, A.P., Smogunov, A., Umari, P., Wentzcovitch, R.M.: QUANTUM ESPRESSO: a modular and open-source software project for quantum simulations of materials. J. Phys.: Condens. Matter **21**, 395502 (2009)
97. Perdew, J.P., Burke, K., Ernzerhof, M.: Generalized gradient approximation made simple. Phys. Rev. Lett. **77**, 3865–3868 (1996)
98. Grimme, S.: Semiempirical GGA-type density functional constructed with a long-range dispersion correction. J. Comp. Chem. **27**, 1787–1799 (2006)
99. Hailegnaw, B., Kirmayer, S., Edri, E., Hodes, G., Cahen, D.: Rain on methylammonium lead iodide based perovskites: possible environmental effects of perovskite solar cells. J. Phys. Chem. Lett. **6**, 1543–1547 (2015)

http://www.springer.com/978-3-319-35112-4

Organic-Inorganic Halide Perovskite Photovoltaics
From Fundamentals to Device Architectures
Park, N.-G.; Grätzel, M.; Miyasaka, T. (Eds.)
2016, VIII, 366 p. 217 illus., 192 illus. in color.,
Hardcover
ISBN: 978-3-319-35112-4